

THE RISE OF MASSIVE RED GALAXIES: THE COLOR–MAGNITUDE AND COLOR–STELLAR MASS DIAGRAMS FOR $z_{\text{phot}} \lesssim 2$ FROM THE MULTIWAVELENGTH SURVEY BY YALE–CHILE (MUSYC)

EDWARD N TAYLOR¹, MARIJN FRANX¹, PIETER G VAN DOKKUM², ERIC F BELL³, GABRIEL B BRAMMER²,
 GREGORY RUDNICK⁴, STIJN WUYTS⁵, ERIC GAWISER⁶, PAULINA LIRA⁷, C MEGAN URRY², HANS-WALTER RIX³,

¹ Sterrewacht Leiden, Leiden University, NL-2300 RA Leiden, Netherlands; ent@strw.leidenuniv.nl,
² Department of Astronomy, Yale University, New Haven, CT 06520-8101, ³ Max-Planck-Institut für Astronomie,
 D-69117 Heidelberg, Germany, ⁴ Goldberg Fellow, National Optical Astronomy Observatories, Tucson, AZ 85721; currently
 at Department of Physics and Astronomy, University of Kansas, Lawrence, KS, 66045 ⁵ W. M. Keck Postdoctoral Fellow,
 Harvard-Smithsonian Center for Astrophysics, Cambridge, MA 02138, ⁶ Department of Physics and Astronomy,
 Rutgers University, Piscataway, NJ, 08854 ⁷ Departamento de Astronomía, Universidad de Chile, Santiago, Chile

Draft version October 31, 2018

ABSTRACT

We present the color–magnitude and color–stellar mass diagrams for galaxies with $z_{\text{phot}} \lesssim 2$, based on a $K^{(\text{AB})} < 22$ catalog of the $\frac{1}{2} \times \frac{1}{2} \square^\circ$ Extended Chandra Deep Field South (ECDFS) from the Multiwavelength Survey by Yale–Chile (MUSYC). Our main sample of 7840 galaxies contains 1297 $M_* > 10^{11} M_\odot$ galaxies in the range $0.2 < z_{\text{phot}} < 1.8$. We show empirically that this catalog is approximately complete for $M_* > 10^{11} M_\odot$ galaxies for $z_{\text{phot}} < 1.8$. For this mass-limited sample, we show that the locus of the red sequence color–stellar mass relation evolves as $\Delta(u-r) \propto (-0.44 \pm 0.02) z_{\text{phot}}$ for $z_{\text{phot}} \lesssim 1.2$. For $z_{\text{phot}} \gtrsim 1.3$, however, we are no longer able to reliably distinguish red and blue subpopulations from the observed color distribution; we show that this would require much deeper near infrared (NIR) data. At $1.5 < z_{\text{phot}} < 1.8$, the comoving number density of $M_* > 10^{11} M_\odot$ galaxies is $\approx 50\%$ of the local value, with a red fraction of $\approx 33\%$. Making a parametric fit to the observed evolution, we find $n_{\text{tot}}(z) \propto (1 + z_{\text{phot}})^{-0.52 \pm 0.12 (\pm 0.20)}$. We find stronger evolution in the red fraction: $f_{\text{red}}(z) \propto (1 + z_{\text{phot}})^{-1.17 \pm 0.18 (\pm 0.21)}$. Through a series of sensitivity analyses, we show that the most important sources of systematic error are: 1. systematic differences in the analysis of the $z \approx 0$ and $z \gg 0$ samples; 2. systematic effects associated with details of the photometric redshift calculation; and 3. uncertainties in the photometric calibration. With this in mind, we show that our results based on photometric redshifts are consistent with a completely independent analysis which does not require redshift information for individual galaxies. Our results suggest that, at most, 1/5 of local red sequence galaxies with $M_* > 10^{11} M_\odot$ were already in place at $z \sim 2$.

Subject headings: Galaxies: Formation — Galaxies: Evolution — Galaxies

1. INTRODUCTION

Observing the evolution of the massive galaxy population provides basic constraints on cosmological models of structure formation, and so helps to identify the physical processes that govern the formation and evolution of massive galaxies. In this context, the color–magnitude diagram (CMD)—astronomy’s most basic diagnostic plot—has been particularly important and useful over the past five years. Physically, a galaxy’s rest-frame color is determined by the (luminosity weighted) mean stellar age, modulo the mean stellar metallicity and extinction from dust in the ISM. The restframe optical brightness acts as a proxy for the total stellar mass, although the connection between the two has a similarly complicated dependence on star formation history, metallicity, and dust. The CMD thus offers two complementary means of characterizing the star formation history of individual galaxies, in terms of the amount and character of their starlight.

In the local universe, galaxies can be separated into two distinct but overlapping populations in color–magnitude space (Baldry et al. 2004): a relatively narrow and well-defined ‘red sequence’, as distinct from the more diffuse ‘blue cloud’, with each following its own color–magnitude relation (CMR). Red sequence galaxies dominate the

bright galaxy population, and tend to have the more concentrated light distributions typical of morphologically early type galaxies (Strateva et al. 2001; Blanton et al. 2003; Driver et al. 2006; Van der Wel 2008). They typically have stellar masses greater than $10^{10.5} M_\odot$ and are dominated by old stars, whereas blue cloud galaxies are typically less massive and continue to be actively star forming (Kauffmann et al. 2003; Brinchmann et al. 2004; Wyder et al. 2007). Further, red sequence galaxies lie preferentially in higher density environments (Hogg et al. 2003; Blanton et al. 2005a; Baldry et al. 2006). The emergent picture is of a population of massive, quiescent, concentrated, and strongly clustered red sequence galaxies, as distinct from the typically less massive, disk-dominated, and star forming blue cloud population (Ellis et al. 2005). This paper focuses on the redshift evolution of the red sequence galaxy population.

Using high quality photometric redshifts from the COMBO-17 survey, Bell et al. (2004b) showed that a red galaxy sequence is already in place at $z_{\text{phot}} \sim 1$ (see also, *e.g.*, Im et al. 2002; Weiner et al. 2005; Willmer et al. 2006). Further, as in the local universe, the $z_{\text{phot}} \approx 0.7$ red sequence is dominated by passive, morphologically early type galaxies (Bell et al. 2004a). The combined mass of red sequence galaxies at $z \sim 1$

is at least half of the present day value (Bell et al. 2004b; Faber et al. 2007; Brown et al. 2008). By contrast, the stellar mass density of actively star forming blue cloud galaxies remains more or less constant for $z \lesssim 1$ (Arnouts et al. 2007; Bell et al. 2007), even as the combined star formation rate drops by an order of magnitude over the same interval (Lilly et al. 1996; Madau et al. 1996; Hopkins 2004). These results—a steadily growing number of passively evolving red galaxies, and a relatively constant number of actively star forming blue galaxies—have led to the idea of a quenching mechanism for star formation, operating to incite a transformation that moves active galaxies from the blue cloud onto the passive red sequence (Menci et al. 2005; Croton et al. 2006; Cattaneo et al. 2006; Dekel & Birnboim 2006; De Lucia et al. 2007).

Our specific goal in this paper is to quantify the evolution of massive galaxies in general, and of red sequence galaxies in particular, in the color–magnitude and color–stellar mass planes for $z_{\text{phot}} \lesssim 2$. The $1 \lesssim z \lesssim 2$ interval is particularly interesting: whereas the $z \sim 1$ galaxy population appears qualitatively similar to the local universe, at least in terms of the existence and properties of red sequence galaxies, the situation at $z \gtrsim 2$ may be quite different. While massive, passive galaxies have been confirmed at $z \gtrsim 1.5$ (Daddi et al. 2005; McGrath et al. 2007) and even $z \gtrsim 2$ (Kriek et al. 2006), these galaxies do not appear to dominate the massive galaxy population as they do at $z \lesssim 1$. Indeed, it appears that the median massive galaxy at $z \sim 2$ has the infrared luminosity of a LIRG or ULIRG (Reddy et al. 2006). Moreover, whereas the number density of massive galaxies at $z \sim 1$ is $\gtrsim 50\%$ of the local value (Juneau et al. 2005; Borch et al. 2006; Scarlata et al. 2007), at $z \gtrsim 2$ it is inferred to be $\lesssim 15\%$ (Fontana et al. 2006; Arnouts et al. 2007; Pozzetti et al. 2007; Pérez-González et al. 2008). This marks the redshift interval $1 \lesssim z \lesssim 2$ as potentially being an era of transition in the universe, in which massive galaxies first begin both to appear in large numbers, and to take on the appearance of their local antecedents. This coincides with end of the period of peak star formation in the universe; while the cosmic star formation rate rises sharply for $z \lesssim 1$, it appears to plateau or even peak for $z \gtrsim 2$ (see, *e.g.*, Hopkins 2004; Nagamine et al. 2006; Panter et al. 2007; Tresse et al. 2007; Pérez-González et al. 2008). Whatever the mechanism that quenches star formation in massive galaxies may be, it is in operation at $1 < z < 2$.

The technical key to gaining access to the $1 \lesssim z \lesssim 2$ universe is deep near infrared (NIR) data (Connolly et al. 1997), since at these redshifts the rest-frame optical features on which both spectroscopic and photometric redshift and stellar mass determinations rely are shifted beyond the observer’s optical window. Moreover, the inclusion of NIR data makes it possible to construct stellar mass limited samples with high completeness (Van Dokkum et al. 2006). Among the next generation of NIR–selected cosmological field galaxy surveys, the Multiwavelength Survey by Yale–Chile (MUSYC; Gawiser et al. 2006) is among the first to become public. MUSYC has targeted four widely dispersed Southern fields, covering a total of one square degree in the $UBVRIz'$ bands. Coupled with this optical imaging pro-

gramme, MUSYC also has two NIR imaging campaigns: a wide ($K^{(\text{AB})} \lesssim 22$) component over three of the four fields (Blanc et al. 2008; Taylor et al. 2008, hereafter Paper I), and a deeper ($K^{(\text{AB})} \lesssim 23.5$) component for four $10' \times 10'$ fields (Quadri et al. 2007).

This present paper focuses on the Extended Chandra Deep Field South (ECDFS), one of the four $\frac{1}{2} \times \frac{1}{2} \square^\circ$ MUSYC fields. Centered on the historical Chandra Deep Field-South ($\alpha = 03^{\text{h}}32^{\text{m}}28^{\text{s}}$, $\delta = -27^\circ48'30''$; J2000 — Giacconi et al. 2001), this is one the best studied fields on the sky, with observations spanning the full electromagnetic spectrum from the X-ray to the radio. Notably, this field is also a part of the COMBO-17 survey (Wolf et al. 2003), and has received *Hubble Space Telescope* ACS coverage as part of the GEMS project (Rix et al. 2004), as well as extremely deep *Spitzer Space Telescope* imaging from the SIMPLE (Damen et al. 2008) project. Further, the GOODS project (Dickinson et al. 2002) covers the $160 \square'$ at the centre of this field, including supporting NIR data from the ISAAC instrument on the VLT (Grazian et al. 2006; Wuyts et al. 2008). Complementing these and other imaging surveys, a wealth of spectroscopic redshifts are available from large campaigns including the K20 survey (Cimatti et al. 2002), the VVDS project (Le Fèvre et al. 2004), the two GOODS spectroscopic campaigns (Vanzella et al. 2008; Popesso et al. 2008), and the IMAGES survey (Ravikumar et al. 2006), among others.

The plan of this paper is as follows. We begin in §2 by giving a brief overview of the data used in this paper — the MUSYC ECDFS dataset itself, as well as the $z \approx 0$ comparison sample from Blanton et al. (2005b). Next, in §3, we describe our basic methods for deriving redshifts and restframe properties for $z \gg 0$ galaxies; our analysis of the $z \approx 0$ comparison sample is described separately in Appendix A. In §4, we construct a stellar-mass limited sample of massive galaxies from our K –selected catalog.

Our basic results — the color–magnitude and color–stellar mass diagrams for $z_{\text{phot}} < 2$ — are presented in §5. We then analyse three separate aspects of the data: evolution in the color distribution of the massive galaxy population in (§6); the color evolution of the red galaxy population as a whole (§7); and the $z_{\text{phot}} \lesssim 2$ evolution in the absolute and relative numbers of massive red/blue galaxies (§8). Our final results are in conflict with those from COMBO-17 in the same field; in Appendix B, we show that this is a product of calibration errors in the COMBO-17 data, rather than differences in our analyses. In §9, we present a series of sensitivity analyses in which we repeat our analysis a number of times, while varying individual aspects of our experimental design, and seeing how these changes affect our results; this tests thus enable us to identify and quantify the most important sources of systematic uncertainty in our main results.

Finally, in §10, we present a completely independent consistency check on our results: we measure the $z \lesssim 2$ evolution of the relative number of bright, red galaxies based only on directly observed quantities — that is, without deriving redshifts or stellar masses for individual galaxies. A summary of our results and conclusions is given in §11.

Throughout this work, magnitudes are expressed in the AB system; exceptions are explicitly marked. All

TABLE 1
SUMMARY OF THE DATA COMPRISING
THE MUSYC ECDFS CATALOG

Band	λ_0 [Å]	Instrument	Exp. Time [min.]	Area [\square']	FWHM	5σ depth (AB)
(1)	(2)	(3)	(4)	(5)	(6)	(7)
<i>U</i>	3560	WFI	1315	973	1''.1	26.5
<i>U₃₈</i>	3660	WFI	825	942	1''.0	26.0
<i>B</i>	4600	WFI	1157	1011	1''.1	26.9
<i>V</i>	5380	WFI	1743	1020	1''.0	26.6
<i>R</i>	6510	WFI	1461	1016	0''.9	26.3
<i>I</i>	8670	WFI	576	976	1''.0	24.8
<i>z'</i>	9070	MOSAIC-II	78	997	1''.1	24.0
<i>J</i>	12500	ISPI	≈ 80	882	$< 1''.5$	23.3
<i>H</i>	16500	Sofi	≈ 60	650	$< 0''.8$	23.0
<i>K</i>	21300	ISPI	≈ 60	887	$< 1''.0$	22.5

NOTE. — For each band, we give the filter identifier (Col. 1) and effective wavelength (Col. 2), as well as the detector name (Col. 3). For the NIR data, exposure times (Col. 4) are given per pointing; the effective seeing (Col. 6) is given for the pointing with the broadest PSF. The 5σ limiting depths (Col. 7) are as measured in $2''.5$ diameter apertures; the smallest apertures we use. The references for each set of imaging data are given in the main text (§2.1).

masses have been derived assuming a ‘diet Salpeter’ IMF (Bell & de Jong 2001), which is defined to be 0.15 dex less massive than a standard Salpeter (1955) IMF. In terms of cosmology, we have assumed $\Omega_\Lambda = 0.70$, $\Omega_m = 0.30$, and $H_0 = 70 \text{ } h_{70} \text{ km s}^{-1} \text{ Mpc}^{-1}$, where $h_{70} = 1$.

2. DATA

2.1. An Overview of the MUSYC ECDFS Dataset

This work is based on a *K*-selected catalog of the ECDFS from the MUSYC wide NIR imaging programme; these data are described and presented in Paper I. We will refer hereafter to this dataset as ‘the’ MUSYC ECDFS catalog, although it should be distinguished from the optical (*B+V+R*)-selected catalog, and the narrow band (5000 Å)-selected photometric catalogs described by Gronwall et al. (2007), and the spectroscopic catalog described by Treister et al. (2008).

The vital statistics of the imaging data that have gone into the MUSYC ECDFS catalog are summarized in Table 1. Unlike the three other MUSYC fields, the ECDFS dataset was founded on existing, publicly available optical imaging: specifically, archival *UU₃₈BVRI* WFI data, including those taken as part of the COMBO-17 survey (Wolf et al. 2003) and ESO’s Deep Public Survey (DPS; Arnouts et al. 2001), which have been re-reduced as part of the GaBoDS project (Erben et al. 2005; Hildebrandt et al. 2006). We also include *H* band imaging (P Barmby, priv. comm.) from Sofi on the 3.6m NTT, covering $\sim 80\%$ of the field, taken to complement the ESO DPS data, reduced and described by Moy et al. (2003).

2.1.1. Original Data Reduction and Calibration

These existing data have been supplemented with original *z'* band imaging from MOSAIC-II, reduced as per Gawiser et al. (2006), as well as *J* and *K* band imaging from ISPI; both instruments are mounted on the

Blanco 4m telescope at CTIO. To cover the full $\frac{1}{2} \times \frac{1}{2} \square^\circ$ ECDFS in the *JK* bands, we have constructed a mosaic of nine $\sim 10 \times 10 \square'$ subfields (the size of the ISPI field of view). The data reduction for the *JK* imaging closely follows Quadri et al. (2007) and Blanc et al. (2008), and is described in detail in Paper I, where we present the MUSYC ECDFS catalog.

In brief, to facilitate multiband photometry, each reduced image has been shifted to a common astrometric reference frame ($0''.267 \text{ pix}^{-1}$). The relative astrometry has been verified to $0''.15$ (0.56 pix). To combat aperture effects (*ie.* similar apertures capturing different fractions of light, due to variable seeing across different images), we have PSF-matched our images to the one with the worst effective seeing. Among the *K* band pointings, the worst effective seeing is $1''.0$ FWHM; this sets our limits for detection and for total *K* band flux measurements. Among the other bands, the worst seeing is $1''.5$ FWHM in the Eastern *J* subfield; this sets the limit for our multicolor photometry. After PSF matching, systematic errors due to aperture effects are estimated to be $\lesssim 0.006$ mag for the smallest apertures we use.

We have tested the photometric calibration through comparison with the COMBO-17 catalog of the ECDFS (Wolf et al. 2003), and with the FIREWORKS catalog of the GOODS-CDFS region (Wuyts et al. 2008). While there are significant differences between the COMBO-17 and MUSYC photometry, the comparison to FIREWORKS validates our photometry and photometric calibration to $\lesssim 0.02$ mag in most cases, particularly for the redder bands. Further, we have tested the relative calibration of all bands using the observed colors of stars; this test validates the photometric cross-calibration to $\lesssim 0.05$ mag. (See §9.1 for a discussion of how sensitive our main results are to photometric calibration errors.)

2.1.2. Photometry

The photometry itself was done using SExtractor (Bertin & Arnouts 1996) in dual image mode, using the $1''.0$ FWHM *K* mosaic as the detection image. Note that, as we were unable to find a combination of SExtractor background estimation parameters (for the detection phase) that were fine enough to map real spatial variations in the background level, but still coarse enough to avoid being influenced by the biggest, brightest sources, we were forced to perform our own background subtraction for the NIR images. Total fluxes were measured from this $1''.0$ *K* image, using SExtractor’s FLUX_AUTO. In Paper I, we show that (in the photometry phase) SExtractor systematically overestimates the background flux level by ~ 0.03 mag; we have taken steps to correct for this effect. Following Labbé et al. (2003), we also apply a minimal correction to account for missed flux beyond the finite AUTO aperture, treating each object as though it were a point source. We quantify the impact these two corrections have on our final results in §9.2.1 and §9.2.2.

Multicolor spectral energy distributions (SEDs) were constructed for each object using the larger of SExtractor’s ISO aperture and a $2''.5$ diameter circular aperture, measured from the $1''.5$ FWHM *U–K* images; we then normalize each object’s SED using the total *K* flux. This flexibility in aperture size is important to compromise between using apertures that are small enough to optimize S:N (the $2''.5$ diameter aperture is close to optimal

in terms of S:N for a point source in the $1''.5$ FWHM J band image), but also large enough to account for color gradients, which are important for the nearest, brightest objects. (See §9.2.3 for a discussion of how our results vary using only fixed aperture photometry to construct SEDs.)

Photometric errors (accounting for sky noise, imperfect background subtraction, etc., as well as the pixel-pixel correlations introduced at various stages in the reduction process) were derived empirically by placing large numbers of ‘empty’ apertures on each image (see also Labbé et al. 2003; Gawiser et al. 2006; Quadri et al. 2007). For the J and K bands, this was done for each subfield individually.

2.1.3. Completeness and Reliability

We have assessed the completeness of the MUSYC catalog of the ECDFS in two ways (Paper I). First, we have tested our ability to recover synthetic, $R^{1/4}$ profile sources of varying total flux and size introduced into empty regions of the data, using procedures identical to ‘live’ detection. This analysis suggests that, at $K = 22$, the MUSYC catalog should be 100 % complete for point sources, dropping to 64 % for $R_{\text{eff}} = 0''.6$ (2.25 pix, or 4.8 kpc at $z = 1$) ellipticals. Secondly, we have compared our catalog to the much deeper FIREWORKS (Wuyts et al. 2008) catalog of the CDFS-GOODS region. In the region of overlap, for $21.8 < K \leq 22.0$ bin, $\gtrsim 85$ % of FIREWORKS detections are found in the MUSYC catalog; all MUSYC detections in this bin are confirmed in the FIREWORKS catalog. Taken together, these two analyses suggest that, at our limiting magnitude of $K = 22$, the MUSYC catalog is primarily magnitude (*cf.* surface brightness) limited, $\gtrsim 85$ % complete, and ~ 100 % reliable.

2.1.4. Sample Selection

In constructing our main galaxy sample, we have identified stars on the basis of the $(B - z') - (z' - K)$ color-color diagram. This selection performs extremely well in comparison with both COMBO-17’s SED classification, and with GEMS point sources (Paper I). We also make three further selections. First, to protect against false detections in regions with lower weights (*e.g.* the mosaic edges, and exposure ‘holes’ in the Eastern K subfield), we require the effective weight in K to be greater than 75 %, corresponding to an effective exposure time of 45 min or more. Secondly, we have masked out, by hand, regions around bright stars where the SEDs of faint objects may be heavily contaminated; this problem is most severe in the z' band, where the PSF has broad wings. With these two selections, the effective area of the catalog becomes $816 \square'$. Thirdly, to protect against extremely poorly constrained redshift solutions, we will limit our analysis to those objects with $S:N > 5$ for the K SED point. (See §9.3.1 for a discussion of how this selection impacts our results.)

Of the 16910 objects in the MUSYC ECDFS catalog, these selections produce 10430 reliable $K \leq 22$ detections, of which 9520 have reliable photometry in the ISPI, MOSAIC-II, and WFI band passes. Of these, 8790 cataloged objects have K S:N > 5 ; 950 of these objects are excluded as stars, leaving 7840 galaxies in our main sample.

2.2. The $z \approx 0$ Comparison Sample

We will investigate the $z_{\text{phot}} \lesssim 2$ evolution in the massive galaxy population by comparing the situation at $z \gg 0$ to that for $z \approx 0$ galaxies in the Sloan Digital Sky Survey (SDSS; York et al. 2000); specifically, we use the ‘low- z ’ sample from the New York University (NYU) Value Added Galaxy Catalog (VAGC) of the SDSS presented by Blanton et al. (2005b). The (Data Release 4) low- z catalog contains *ugriz* photometry for 49968 galaxies with $10 < D < 150$ Mpc ($z_{\text{spec}} \lesssim 0.05$), covering an effective area of $6670 \square^\circ$; 2513 of these galaxies have $M_* > 10^{11} M_\odot$. Our analysis of these data closely follows that of the $z \gg 0$ sample, and is described separately in Appendix A.

3. PHOTOMETRIC REDSHIFTS AND RESTFRAME PROPERTIES

3.1. Photometric Redshifts

The technical crux on which any photometric look-back study rests is the determination of redshifts from broadband SEDs. We have computed our photometric redshifts using EAZY (Brammer et al. 2008), a new, fully-featured, user-friendly, and publicly-available photometric redshift code. By default, the z_{phot} calculation is based on all ten bands, although we do require that the effective weight in any given band is greater than 0.6; in practice, this requirement only affects the H band, where we do not have full coverage of the field. The characteristic filter response curves we use account for both atmospheric extinction and CCD response efficiency as a function of wavelength.

For our fiducial or default analysis, we simply adopt the recommended default settings for EAZY: *viz.*, we adopt the EAZY default redshift and wavelength grids, template library, template combination method, template error function, K luminosity prior, etc. (See Brammer et al. 2008, for a complete description.) Note that, by default, EAZY assigns each object a redshift by marginalizing over the full probability distribution rather than, say, through χ^2 minimization. For this work, a key feature of EAZY is the control it offers over how the SED fitting is done: the user is able to specify whether and how the basic template spectra are combined, whether or not to include luminosity prior and/or a template error function, and how the output redshift is chosen. We will make use of EAZY’s versatility in §9.4 to explore how these particular choices affect our results.

One of the unique aspects of the ECDFS is the high number of publicly available spectroscopic redshift determinations, which can be used to validate and/or calibrate our photometric redshifts. In Paper I, we describe a compilation of spectroscopic redshifts for 2914 unique objects in our catalog, including ‘robust’ redshifts for 1656 galaxies in our main $K < 22$ sample. These redshifts come from some of the many literature sources available in the ECDFS, including those large surveys referred to in §1, as well as the X-ray selected spectroscopic redshift catalogs of Szokoly et al. (2004) and Treister et al. (2008), a new survey by S Kopev et al. (in prep.), and a number of smaller projects. K20 is particularly useful in this regard, given its exceptionally high spectroscopic completeness, albeit over a very small area: 92 % of $K^{(\text{Vega})} < 20$ sources over $52 \square'$.

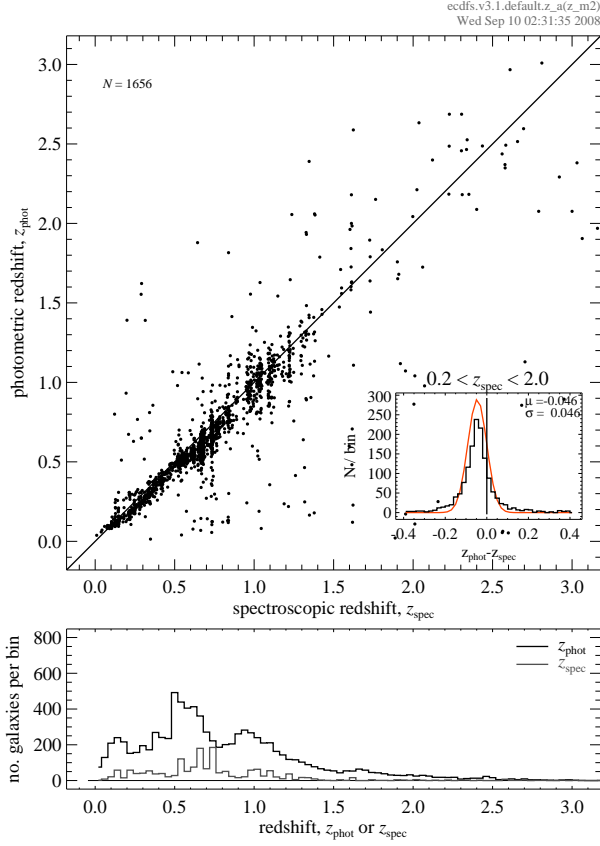


FIG. 1.— Validating the MUSYC catalog photometric redshift determinations—*Main panel*: the $z_{\text{spec}}-z_{\text{phot}}$ diagram for the 1656 galaxies from our main $K < 22$ sample, using a compendium of ‘robust’ spectroscopic redshifts from the literature (see Paper I). *Inset*: the distribution of $\Delta z = z_{\text{phot}} - z_{\text{spec}}$ for the same set of galaxies; the curve shows a Gaussian fit to this distribution, with parameters as given. *Lower panel*: the redshift distributions of the main and spec- z samples; our photometric redshifts appear to mildly underestimate the redshift of the three overdensities at $0.5 < z_{\text{spec}} < 0.8$. Quantitatively, we find the median and NMAD of $\Delta z/(1 + z_{\text{spec}})$ for the full spec- z sample to be -0.029 and 0.036 , respectively (See also Figure 2); for $z_{\text{spec}} > 1$, we find these numbers to be -0.023 and 0.060 ; for the K20 sample, which is 92 % complete for $K^{(\text{AB})} < 21.8$, these numbers are -0.028 and 0.033 .

The main panel of Figure 1 shows our $z_{\text{spec}}-z_{\text{phot}}$ plot. We prefer to quantify the photometric redshift quality in terms of the normalized median absolute deviation (NMAD¹) in $\Delta z/(1 + z_{\text{spec}})$, which we will abbreviate as σ_z ; for this comparison sample, $\sigma_z = 0.035$. Further, the outlier fraction is acceptably small: 5.9 %. Comparing only to the 241 redshifts from K20, we find $\sigma_z = 0.033$; for the Van der Wel et al. (2005) sample of 28 $z \sim 1$ early type galaxies the figure is 0.022. For $1 < z_{\text{spec}} < 2$, we find $\sigma_z = 0.059$. For the 20 % (269/1297) of $0.2 < z_{\text{phot}} < 1.8$ galaxies from our mass limited sample defined in §4 that have spectroscopic redshifts, we find $\sigma_z = 0.043$.

Based on their catalog of the GOODS ACS and ISAAC data, Grazian et al. (2006) have achieved a photometric redshift accuracy of $\langle \Delta z/(1 + z_{\text{spec}}) \rangle$ of 0.045. For comparison to Grazian et al. (2006), the inset panel shows

the distribution of $\Delta z = (z_{\text{phot}} - z_{\text{spec}})$ for $0 < z_{\text{spec}} < 2$; although offset by -0.046 , the best fit Gaussian to the distribution has a width of 0.046, as opposed to 0.06 for Grazian et al. (2006). For an identical sample of 938 galaxies with $z_{\text{spec}}\text{s}$, we find $\sigma_z = 0.043$ for the Grazian et al. (2006) $z_{\text{phot}}\text{s}$ and $\sigma_z = 0.035$ for ours. In other words, our photometric redshift determinations are at least as good as the best published for K -selected samples at high redshifts. We also note in passing that our $z_{\text{phot}} \lesssim 1$ photometric redshifts agree very well with those from COMBO-17 (Wolf et al. 2003); a detailed comparison to both these catalogs is presented in Paper I.

The lower panel of Figure 1 shows the redshift distributions for both our main galaxy sample (based on z_{phot}), and the spectroscopic comparison sample (based on z_{spec}). Note the presence of three prominent redshift spikes at $0.5 < z_{\text{spec}} < 0.8$ (see also Vanzella et al. 2008); it appears that our redshift determinations may slightly underestimate the redshifts of these structures. The structures at $z \sim 1.0, 1.1, 1.2, 1.3$, and 1.4 (Vanzella et al. 2008) are also visible in the z_{spec} distribution, but are ‘washed out’ in the z_{phot} distribution.

3.2. Restframe Photometry and Stellar Masses

The many degeneracies between SED shape and the intrinsic properties of the underlying stellar population, which are actually a help when deriving photometric redshifts, make the estimation of such properties from SED fitting highly problematic. Systematic uncertainties associated with parameterisations of the assumed star formation history are at the level of 0.1 dex (Pozzetti et al. 2007), while uncertainties in the stellar population models themselves are generally accepted to be $\lesssim 0.3$ dex; this is comparable to the uncertainty associated with the choice of stellar IMF. For these reasons, we have opted for considerably simpler means of deriving restframe parameters.

Once the redshift is determined, we have interpolated restframe fluxes from the observed SED using a new utility dubbed InterRest, which is a slightly more sophisticated version of the algorithm described in Appendix C of Rudnick et al. (2003), and is described in detail in Paper I. InterRest is designed to dovetail with EAZY, and is also freely available.² We estimate the systematic errors in our interpolated fluxes (*cf.* colors) to be less than 2 % (Paper I).

We then use this interpolated restframe photometry to estimate galaxies’ stellar masses using a prescription from Bell & de Jong (2001), which is a simple linear relation between restframe $(B - V)$ color and stellar mass-to-light ratio: M_*/L_V :

$$\log_{10} M_*/L_V = -0.734 + 1.404 \times (B - V + 0.084), \quad (1)$$

assuming $M_{V,\odot} = 4.82$. (Here, the factor of 0.084 is to transform from the Vega magnitude system used by Bell & de Jong (2001) to the AB system used in this work.) This prescription assumes a ‘diet Salpeter’ IMF, which is defined to be 0.15 dex less massive than the standard Salpeter (1955) IMF, and is approximately 0.04 dex more massive than that of Kroupa (2001). Further,

¹ The NMAD is defined as $1.48 \times \text{median}[|x - \text{median}(x)|]$; the normalization factor of 1.48 ensures that the NMAD of a Gaussian distribution is equal to its standard deviation.

² Code and documentation can be found at: <http://www.strw.leidenuniv.nl/~ent/InterRest/>.

to prevent the most egregious overestimates of stellar masses, we limit $M_*/L_V \leq 10$ (see also Figure 4 of Borch et al. 2006). Although this limit affects just 1.2 % of our main sample, we found it to be important for getting the high-mass end of the $z \approx 0$ mass function right (Appendix A).

It is not immediately obvious whether using these color-derived M/L s is significantly better or worse than, say, from using stellar population synthesis to fit the whole observed SED. The prescription we use has been derived from SED-fit M/L s; the scatter around this relation is on the order of 0.1 dex. By comparison, the precision of SED-fit M/L determinations is limited to 0.2 dex by degeneracies between, *e.g.*, age, metallicity, and dust obscuration (see, *e.g.*, Pozzetti et al. 2007; Conselice et al. 2007). Thus, the increase in the random error in M_* due to the use of color-derived rather than SED-fit stellar masses is ~ 10 %.

In addition to being both simpler and more transparent, however, the use of color-derived M/L s has the major advantage of using the same restframe information for all galaxies, irrespective of redshift. This is especially important when it comes to the comparison between the high- z and low- z samples, where the available photometry samples quite different regions of the restframe spectrum. Since Equation 1 has ultimately been derived from SED-fit mass estimates, however, our color-derived mass estimates are still subject to the same systematic uncertainties. To the extent that such systematic effects are independent of color, redshift, etc., they can be accommodated within our results by simply scaling our limiting mass. On the other hand, if there is significant evolution in the color- M/L relation with redshift, then there is the risk that the use of color-derived M/L s may introduce serious systematic errors with redshift. We investigate this issue further in §9.5, in which we also demonstrate that our results are essentially unchanged if we use conventional SED-fitting techniques to derive M/L s.

3.3. The Propagation of Redshift Errors

A primary concern in this paper is the importance of systematic errors. To address this concern in the context of our photometric redshift determinations, we show in the top panels of Figure 2 the $z_{\text{spec}} - z_{\text{phot}}$ agreement as a function of redshift, S:N in the K ‘color’ aperture, and restframe color. In each panel, the points with error bars show the median and 15/85 percentiles in discrete bins.

Looking first at our photometric redshifts: the first panel of Figure 2, shows the photometric redshift error, $\Delta z/(1+z_{\text{spec}})$, as a function of z_{spec} . We see that there is a systematic offset between z_{phot} and z_{spec} for $z_{\text{spec}} \lesssim 1$, such that our z_{phot} s tend to be slightly too low (see also Figure 1); for $z \gtrsim 1$, this effect appears to be less. At least for K S:N $\gtrsim 10$, random errors in the photometric redshifts do not appear to be a strong function of S:N.

There is a clear systematic effect as a function of restframe color. For galaxies redder than $(u-r) \approx 2$ (approximately the lower limit for $z \approx 0$ red sequence galaxies), the agreement between z_{phot} and z_{spec} is very good. For galaxies with $(u-r) \lesssim 2$, however, it seems that we systematically underestimate the true redshift by approximately $\Delta z \lesssim 0.02(1+z_{\text{spec}})$. It is plausible that this is in fact the driver of the weak apparent systematic effect with redshift, coupled with there being a greater

proportion of blue galaxies in the spectroscopic redshift sample at lower redshifts.

How do these errors in redshift estimation play out in the derivation of restframe properties? We address this question with reference to the lower panels of Figure 2, which illustrate how redshift uncertainties affect our derivation of three basic restframe quantities (*top to bottom*): absolute luminosity, restframe color, and stellar mass. In each panel, we plot the difference between the values derived adopting the spectroscopic or photometric redshift, as a function of (*left to right*) redshift, K band S:N, and restframe color, as well as photometric redshift error.

Quantitatively, for our z_{spec} comparison sample, the random photometric redshift error of $\Delta z/(1+z_{\text{spec}}) = 0.035$ translates into a 0.360 mag error in absolute magnitude, 0.134 mag error in restframe color, and a 0.107 dex error in stellar mass. (By contrast, the typical uncertainty in for a K S:N = 10 galaxy is $\Delta K = 0.12$ – 0.16 mag ≈ 0.05 – 0.07 dex.) Just as for the redshifts themselves, the clearest systematic effects in the derived quantities is with restframe color: there appear to be mild systematics with redshift for $z \lesssim 1$, and no clear trend with S:N, at least for S:N > 10.

It is straightforward to understand why redshift errors play a larger role in the derivation of magnitudes rather than colors. When calculating magnitudes, the primary importance of the redshift is a distance indicator. For the z_{spec} sample shown in Figure 2, the random scatter in ΔM_r due to distance errors alone (calculated by taking the difference in the distance modulus implied by z_{phot} versus that by z_{spec}) is 0.28 mag; *ie.* ~ 75 % of the scatter seen in Figure 2. On the other hand, colors are distance independent, and this element of uncertainty is cancelled out.

What is surprising is the relative insensitivity of our stellar mass estimates to redshift errors. Focusing on the right panels of Figure 2, it can be seen that where the photometric redshift underestimates the true redshift/distance, we will infer both too faint an absolute luminosity and too red a restframe color. When it comes to computing a stellar mass, however, these two effects operate in opposite directions: although the luminosity is underestimated, the too-red color leads to an overestimate of the stellar mass-to-light ratio. The two effects thus partially cancel one another, leaving stellar mass estimates relatively robust to redshift errors.

In a photometric redshift survey, the measurement uncertainty *due to random photometric redshift errors* is considerably less for stellar masses than it is for absolute magnitudes. This conclusion remains unchanged using SED-fit stellar masses, rather than our favored color-derived ones. Conversely, we can say that (random) photometric redshift errors are not a dominant source of uncertainty in our stellar mass estimates. Indeed, as we have already noted, the size of these errors is comparable to the uncertainties in our total flux measurements.

4. CONSTRUCTING A STELLAR MASS SELECTED SAMPLE

For moderate to high redshifts, NIR selection has the key advantage of probing the restframe optical light, which is a reasonable tracer of stellar mass. In this

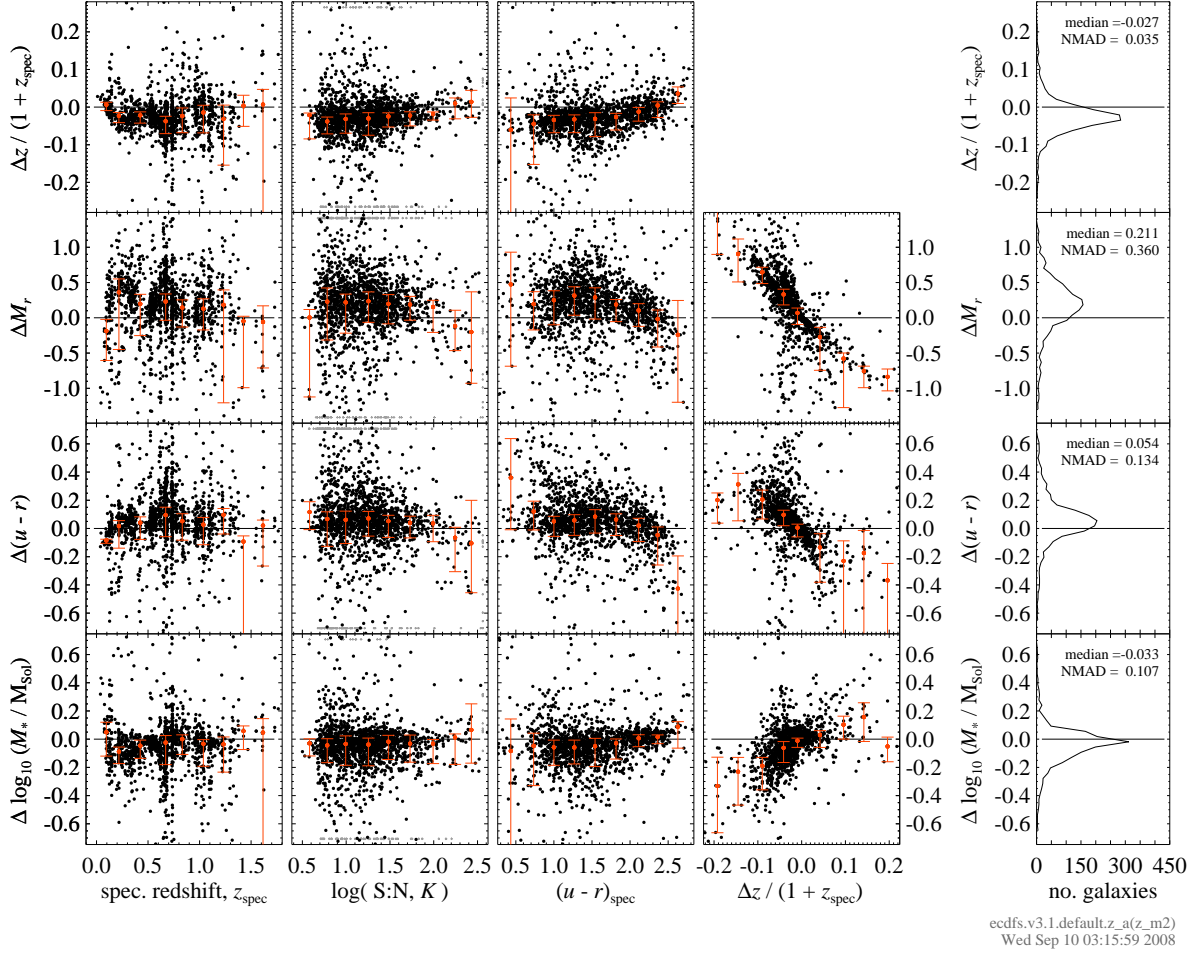


FIG. 2.— Photometric redshift errors, and their effect on other derived quantities—In each panel, the abscissa shows the difference in a derived quantity, derived assuming the spectroscopic or photometric redshift; in all cases, ‘ Δ ’ should be understood as the difference between the z_{phot} minus z_{spec} -derived values. We show: (top to bottom, in rows) redshift, absolute magnitude, restframe color, and stellar mass, as a function of (left to right, in columns) redshift, observed signal-to-noise, restframe color, and photometric redshift error. The black points are for the spectroscopic sample shown in Figure 1; the red points show the median offset in bins; the error bars reflect the 15/85 percentiles. In each panel, points that fall outside of the plotted range are shown as small grey plusses. The separate panels at right show the distribution of Δ s for all galaxies in the z_{spec} sample; the median and scatter (NMAD) in the difference between z_{phot} - and z_{spec} -derived quantities are as shown. In all cases, the clearest systematic effects are as a function of redshift, with some systematic errors for the reddest and bluest galaxies. The way that redshift errors propagate mean that the uncertainties due to redshift errors are much smaller for stellar masses than they are for either absolute magnitudes or restframe colors.

section, we empirically relate our observed flux detection/selection limit to an approximate completeness limit in terms of stellar mass and redshift.

To this end, we have taken galaxies with K fluxes immediately below our detection limit from three significantly deeper K -selected catalogs; *viz.* the MUSYC deep NIR catalogs (Quadri et al. 2007), the FIREWORKS catalog (Wuyts et al. 2008), and the FIRES catalogs (Labbé et al. 2003; Förster-Schreiber et al. 2006). By taking objects from these catalogs that lie immediately below our detection threshold, and scaling their fluxes (and so stellar masses) to match our $K = 22$ limit, it is then possible to empirically determine the stellar mass–redshift relation for $K \approx 22$ galaxies. The upper envelope of points in (M_*, z_{phot}) space thus represents the most massive galaxies at our observed flux limit, and so directly provides a redshift-dependent mass completeness limit.

This is illustrated in the left panel of Figure 3. In

this panel, the large, open, colored symbols represent $22.0 < K < 22.5$ objects from the deeper catalogs, scaled up in flux to $K = 22$; *viz.* the MUSYC deep NIR catalogs (blue crosses), the FIREWORKS catalog (yellow circles), and the FIRES catalogs (red squares). Again, these points represent objects immediately at our detection limit; the upper envelope of these points therefore represents the most massive galaxies that might escape detection/selection in our analysis. This suggests that for $M_* > 10^{11} M_\odot$, we are approximately complete for $z_{\text{phot}} < 1.8$.

It is possible to do the same thing using the faintest detections from our own catalog, scaled down in flux to our selection limit. Specifically, we have taken galaxies with $21.5 < K < 22.0$ and scaled their fluxes (and masses) down to $K = 22$. For this test, we also restrict our attention to galaxies with well constrained redshifts, by requiring that the EAZY ‘odds’ parameter be greater than 0.95.

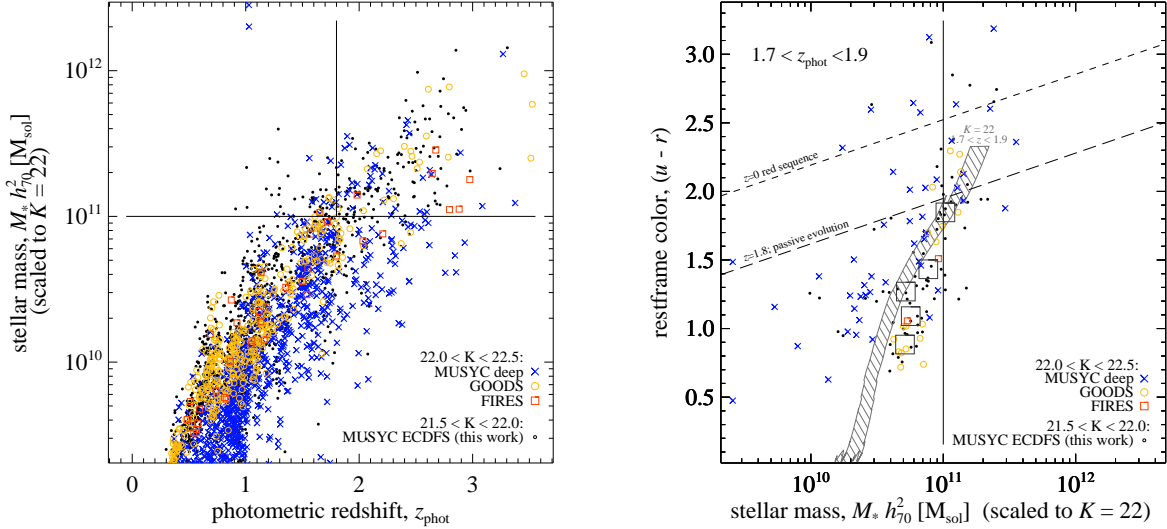


FIG. 3.— Empirically determining our mass completeness limit as a function of redshift—*Left panel*— The black points show stellar masses for MUSYC ECDFS galaxies with $21.5 < K < 22.0$, scaled down in flux to match our $K = 22$ detection limit, and plotted as a function of photometric redshift. The other symbols show stellar masses for $22.5 > K > 22.0$ galaxies, scaled up in flux to $K = 22$; these galaxies are drawn from the MUSYC deep fields (blue crosses), the FIREWORKS catalog (yellow circles), and the FIRES catalogs (red squares). Each sample has been analyzed in exactly the same manner. The upper envelope of these points effectively defines, as a function of redshift, the limiting stellar mass corresponding to our observed K flux limit. For $M_* > 10^{11} M_\odot$, we are nearly complete ($\gtrsim 90\%$) to $z_{\text{phot}} = 1.8$. *Right panel*—the color–stellar mass diagram for $K \approx 22$ galaxies at $1.7 < z_{\text{phot}} < 1.9$ —the large squares show the median values for the MUSYC ECDFS points, binned by color; all other symbols are as in the left panel. Here, the right envelope of the colored points defines our mass completeness limit at $z_{\text{phot}} \approx 1.8$ as a function of color. For comparison with Figures 4 and 5, the hatched region shows estimated completeness limits based on synthetic SSP spectra. While we may well miss galaxies considerably redder than the predicted red sequence (see §7), at $z_{\text{phot}} \approx 1.8$, this empirical argument suggests that we are approximately complete ($\gtrsim 85\%$) for galaxies with $M_* > 10^{11} M_\odot$ and $(u-r) < 2$.

These points are shown as the closed circles in the left panel of Figure 3. While the results of this ‘internal’ test are broadly consistent with the previous ‘external’ one, they do suggest slightly higher incompleteness. Of the $21.5 < K < 22.0$ sources with $1.6 < z_{\text{phot}} < 1.8$, 23 % (20/87) would have $M_* > 10^{11} M_\odot$ when scaled down to $K = 22$, indicating that our completeness for $K = 22$, $M_* = 10^{11} M_\odot$ galaxies is $\sim 75\%$ for $1.6 < z_{\text{phot}} < 1.8$. However, the $21.5 < K < 22.0$ subsample shown here represents only 30 % of our full $K < 22$ sample in this mass and redshift range, suggesting that the overall completeness is more like $> 90\%$.

As a second and complimentary check on this conclusion, the right panel of Figure 3 shows the color–stellar mass diagram for a narrow redshift slice at $1.7 < z_{\text{phot}} < 1.9$. Here, the large squares show the median values from the MUSYC ECDFS points, binned by color; the other symbols are the same as in the other panel of this Figure. As before, the points in this panel represent objects at our detection limit; the right envelope of these points thus describes our mass completeness limit for $z_{\text{phot}} \approx 1.8$, this time as a function of restframe color.

Again, the ‘internal’ and ‘external’ analyses broadly agree. For blue galaxies, both tests suggest that MUSYC should be very nearly complete for $M_* > 10^{11} M_\odot$ and $z_{\text{phot}} < 1.8$. For $(u-r) > 1.5$ galaxies, however, the down-scaled MUSYC points again suggest slightly lower completeness than those scaled up from deeper catalogs: 45 % (13/29) of these galaxies would fall foul of one of our selection criteria if their masses were scaled down to

$M_* = 10^{11} M_\odot$. Using an argument analogous to that above, this suggests that our completeness fraction for galaxies with $M_* > 10^{11} M_\odot$, $z_{\text{phot}} = 1.8$, and $(u-r) > 1.5$ is at least $\sim 85\%$.

We therefore adopt $M_* > 10^{11} M_\odot$ and $z_{\text{phot}} < 1.8$ as our approximate completeness limits, corresponding to our $K < 22$ detection/selection limit. In §9.3.2, we apply simple completeness corrections to determine the extent to which our results may be affected by incompleteness. As a final caveat, however, there remains the concern of additional incompleteness due to our K S:N > 5 criterion, which we will address in §9.3.1.

5. THE COLOR–MAGNITUDE AND COLOR–STELLAR MASS DIAGRAMS FOR $z_{\text{phot}} \lesssim 2$

In this section, we present our basic observational results: the color–magnitude and color–stellar mass diagrams for $z_{\text{phot}} \lesssim 2$.

5.1. The Color–Magnitude Diagram for $z_{\text{phot}} \lesssim 2$

Figure 4 shows the color–magnitude diagram (CMD), plotted in terms of $(u-r)$ color and absolute r magnitude, M_r , for $z_{\text{phot}} \lesssim 2$.

The first panel of Figure 4 is for $z \approx 0$ galaxies from the ‘low- z ’ comparison sample; these data and our analysis of them are described in Appendix A. The basic features of the CMD — the red sequence, blue cloud, and green valley — are all easily discernible. The dotted line shows our characterization of the $z \approx 0$ CMR for red galaxies (Equation A1), also discussed in Appendix A.

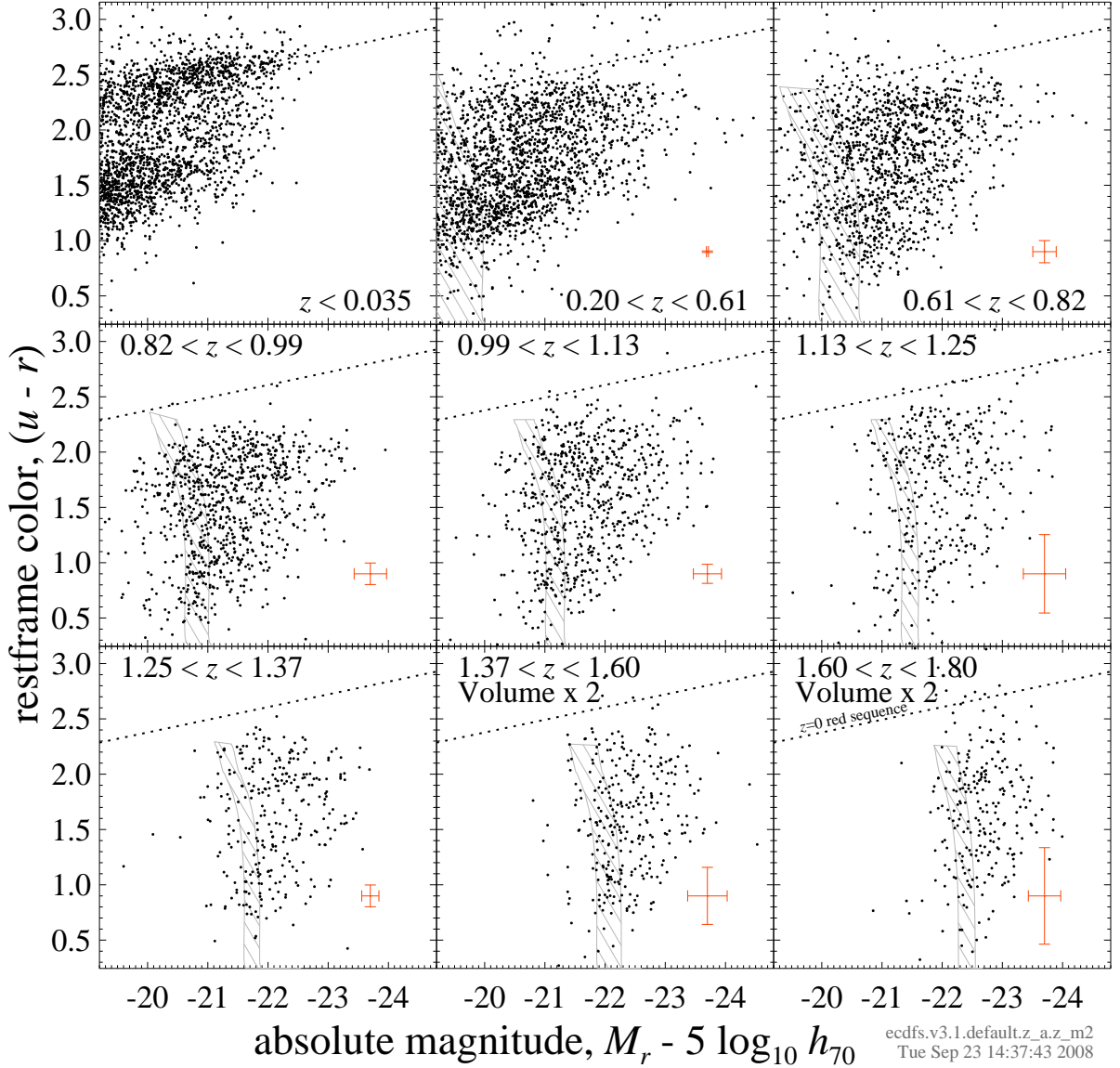


FIG. 4.— The color–magnitude diagram (CMD) for galaxies with $z_{\text{phot}} \lesssim 2$ — The first panel shows a random selection from the NYU VAGC’s ‘low- z ’ sample, based on DR4 of the SDSS (Blanton et al. 2005b), discussed in Appendix A; the other panels show the MUSYC ECDFS data, discussed in the main text. Except where marked, bins are of equal comoving volume; for the low- z sample, we have plotted a random sub-sample to yield the same effective volume: the density of points is thus directly related to bivariate comoving number density. The shaded area shows the approximate $K = 22$ detection/selection limits, based on synthetic spectra for an SSP; the error bars show representative errors for a $M_* \approx 10^{11} M_\odot$, $(u-r) \approx 2.0$ galaxy at the mean redshift of each bin. The dotted line in each panel shows our fit to the CMR for bright, red sequence galaxies at $z \approx 0$, derived in Appendix A. In this work, we prefer to use stellar mass, rather than absolute magnitude, as a basic parameter—accordingly, we focus our attention on the CM_{*}D, presented in Figure 5.

The other eight panels show the $0.2 < z_{\text{phot}} < 1.8$ MUSYC ECDFS data. Except for the two highest redshift bins, which are twice as large, the $z_{\text{phot}} \gg 0$ bins have been chosen to have equal comoving volume.³ For the $z \approx 0$ bin, we plot only a random sub-sample of the low- z catalog, chosen to effectively match the volume of the higher redshift bins. Thus, the density of points in the color–magnitude plane is directly related to changes in the bivariate comoving number density.

In the bottom-right corner of each panel, we show rep-

resentative error bars for a $M_* \approx 10^{11} M_\odot$ galaxy with $(u-r) \approx 2.0$, near the mean redshift of each bin. In order to derive these errors, we have created 100 Monte Carlo realizations of our catalog, in which we have perturbed the catalog photometry according to the photometric errors, and repeated our analysis for each: the error bars show the scatter in the values so derived. The shaded grey regions show approximately how our $K < 22$ completeness limit projects onto color–magnitude space through each redshift bin, derived using synthetic single stellar population (SSP) spectra.

Examining this diagram it is clear that, in the most general terms possible, bright/massive galaxies were considerably bluer in the past. At a fixed magnitude, the

³ The exact redshift limits we have used are $z_{\text{phot}} = 0.200, 0.609, 0.825, 0.987, 1.127, 1.254, 1.373, 1.486, 1.595, 1.700, 1.804, 1.906$, and 2.000; elsewhere we will round these values as convenient.

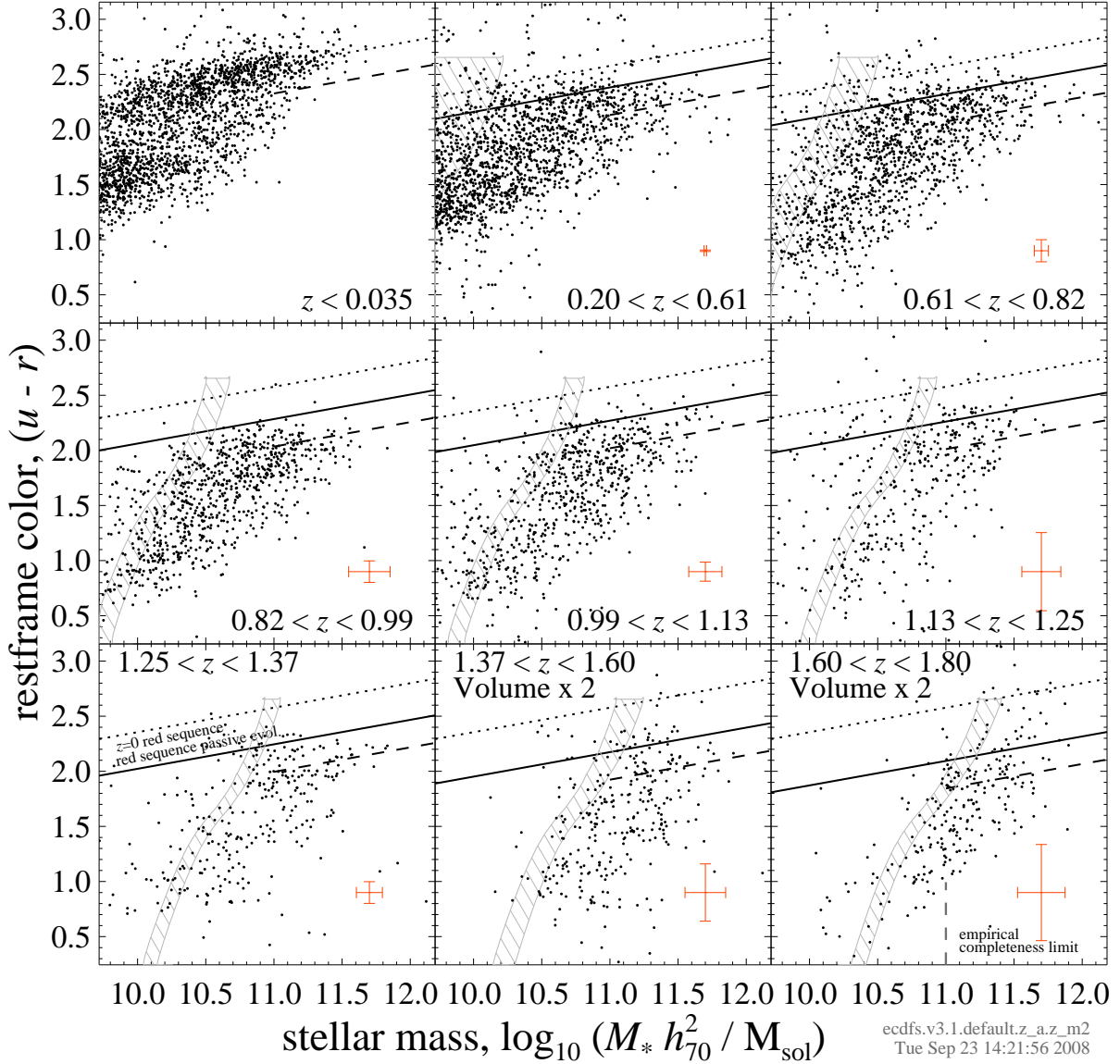


FIG. 5.— The color–stellar mass diagram (CM*D) for galaxies with $z_{\text{phot}} \lesssim 2$ — As in Figure 4, the $z \approx 0$ bin is based on the low- z sample of SDSS galaxies, discussed in Appendix A; the $z_{\text{phot}} \gg 0$ points based on the MUSYC ECDFS data, described in the main text. The hatched area shows approximate selection limits, based on synthetic spectra for an SSP; our empirical completeness limit is marked in the last bin. The error bars show representative errors for a $M_* \approx 10^{11} M_\odot$, $(u-r) \approx 2.0$ galaxy near the bin’s mean redshift, based on 100 Monte Carlo realizations of the catalog data, including photometric redshift errors. Within each panel, the dotted line shows our fit to the CM*R for bright red sequence galaxies at $z \approx 0$, derived as per Appendix A; for the $z_{\text{phot}} \gg 0$ bins, the solid lines show our fit to the color evolution of the massive red galaxy population, derived in §7; the dashed line shows our red galaxy selection criterion, introduced in §8. We analyse the key features of this diagram further in Figures 6, 8, 9, and 10.

entire $z \sim 1$ galaxy population is a few tenths of a magnitude bluer than at $z \approx 0$. At the same time, particularly for $z \gtrsim 1$, there is a growing population of galaxies with $M_r < -22$ and $(u-r) < 2$ that has no local analogue. While there are some indications of a red sequence within the $z \gg 0$ data, particularly for $z_{\text{phot}} \lesssim 1$, it is certainly not so easily distinguishable as locally.

5.2. The Color–Stellar Mass Diagram for $z_{\text{phot}} \lesssim 2$

There are a number of advantages to using stellar mass as a basic parameter, rather than absolute magnitude. Principal among these is the fact that stellar mass is more directly linked to a galaxy’s growth and/or assembly: while a galaxy’s brightness will wax and wane with

successive star formation episodes, a galaxy’s evolution in stellar mass is more nearly monotonic. On the other hand, it must be remembered that the necessary assumptions in the derivation of stellar mass estimates produce greater systematic uncertainties than for absolute luminosities. As bursts of star formation and other aspects of differing star formation histories among galaxies are likely greater at higher redshifts, however, we will focus on the color–stellar mass diagram in this and following sections.

Figure 5 shows the color–stellar mass diagram (CM*D) for $z \lesssim 2$. As in Figure 4, the first panel shows a random sub-sample of the low- z sample; the other panels show the MUSYC ECDFS data. The dotted line in each panel

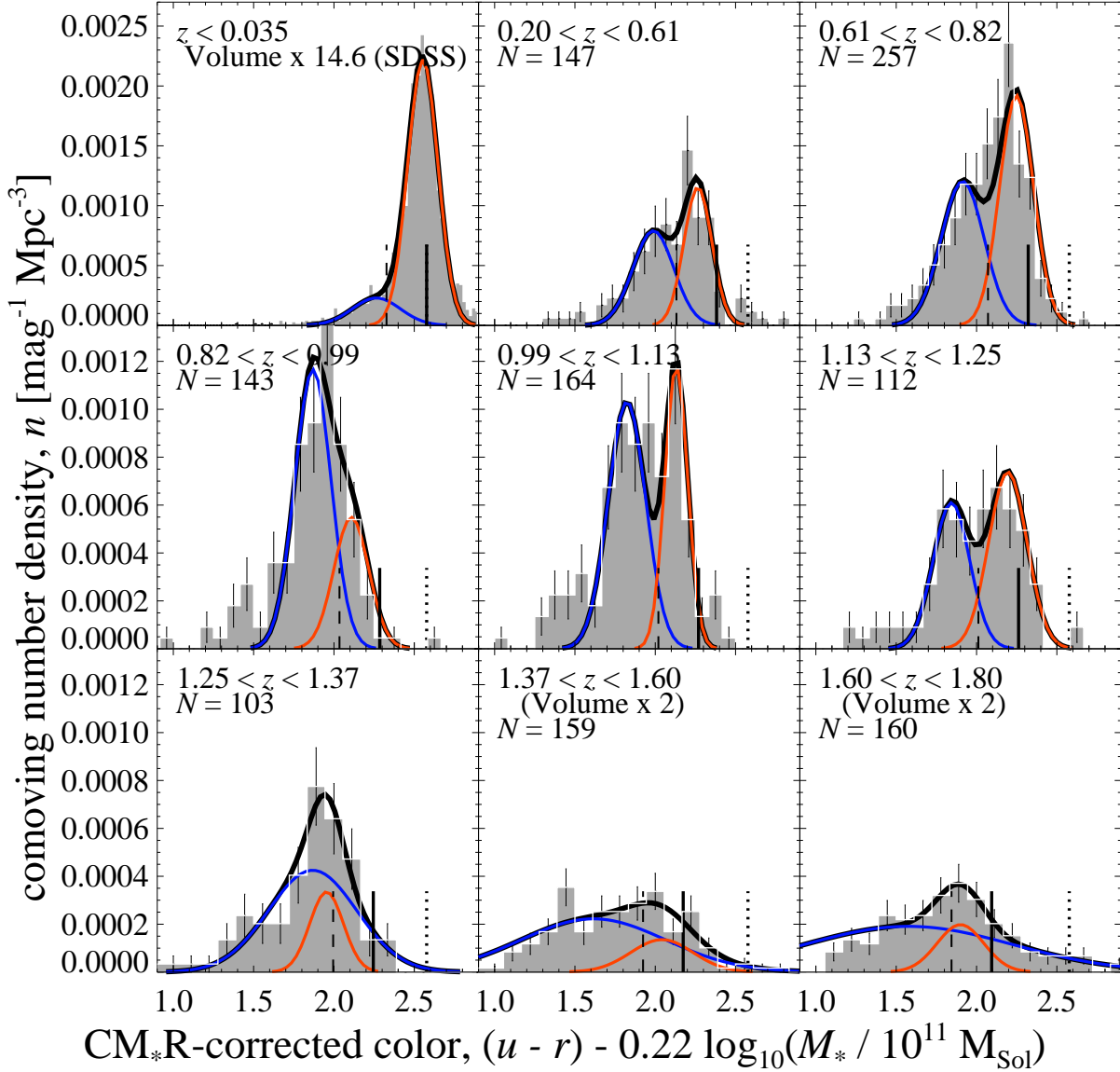


FIG. 6.— Color distributions for $M_* > 10^{11} M_\odot$ galaxies at $z \lesssim 2$ — In each panel, the histograms show the color distribution for $M_* > 10^{11} M_\odot$ galaxies, after subtracting out the slope of the local CM_*R , normalized at $M_* = 10^{11} M_\odot$. The shaded distributions show the data themselves. The smooth curves show double Gaussian fits to the observed distributions. For $z_{\text{phot}} \gtrsim 1.2$, the Gaussian fits to the observed color distributions are not robust; our inability to reliably distinguish separate red and blue populations for $z_{\text{phot}} \gtrsim 1.2$ is likely due to insufficient S:N in our NIR data (see Figure 7). In each panel, the vertical dotted line shows the location of the $z \approx 0$ red sequence; the vertical solid lines show our fit to the observed color evolution of the red sequence, derived in §7; the dashed lines show our red galaxy selection criterion, introduced in §8.

shows the $z \approx 0$ color–stellar mass relation (CM_*R), which we have derived in Appendix A, given in Equation A1.

Each of the basic features of the CMD are also seen in the CM_*D . We see an increasing number of galaxies with $z_{\text{phot}} \gtrsim 1$ and with $M_* > 10^{11} M_\odot$ and $(u - r) \lesssim 2$ which have no analogues in the local universe. For a SSP, the colors of these galaxies would suggest ages of $\lesssim 1$ Gyr: these massive galaxies appear to be in the throes of their final star formation episodes. For $z_{\text{phot}} \gtrsim 1.2$, these galaxies may even dominate the massive galaxy population. Some evidence for a distinct red sequence is visible in the CM_*D for $z_{\text{phot}} \lesssim 1$, but not much beyond.

The next three sections are devoted to more quantitative discussion of each of the following three specific

observations:

1. We see evidence for a red galaxy sequence for $z_{\text{phot}} \lesssim 1.2$; beyond this redshift, whether due to physical evolution or to observational errors, it becomes impossible to unambiguously identify a distinct red sequence on the basis of the present data (§6).
2. At a fixed mass, a red sequence galaxy at $z \sim 1$ is a few tenths of a magnitude bluer than its $z \sim 0$ counterpart (§7).
3. At higher redshifts, there appear to be fewer massive galaxies on the red sequence. Further, it appears that the proportion of blue cloud galaxies

among the most massive galaxies increases; conversely, the red fraction is lower at higher redshifts. (§8).

6. THE COLOR DISTRIBUTION OF MASSIVE GALAXIES FOR $z_{\text{phot}} < 2$

In an attempt to quantitatively separate the massive galaxy population into distinct red and blue sub-populations, Figure 6 plots the color distribution of the $M_* > 10^{11} M_\odot$ galaxy population, after subtracting out the slope of the $z \approx 0$ CM*R, and using the same redshift bins as in Figures 4 and 5. The grey histograms in each panel show the data themselves. Note that for the $z \approx 0$ panel of this plot, we have used the full low- z sample. Also, recall that for this mass regime, we are approximately complete (volume limited) to $z_{\text{phot}} = 1.8$.

6.1. The Massive Galaxy Red Sequence at $z_{\text{phot}} \lesssim 1.2$

Locally, red sequence galaxies totally dominate the massive galaxy population: what bimodality exists between the red and blue populations is weak. (As the name suggests, ‘bimodality’ implies two distinct local maxima in the distribution.) This is a reflection of the apparent ‘transition mass’ between red and blue galaxies observed by Kauffmann et al. (2003); the bimodality is stronger in a luminosity limited sample, including a greater proportion of bright but less massive blue cloud galaxies (see also Figure A1; Appendix A). At slightly higher redshifts, where some progenitors of $z \approx 0$ red sequence galaxies are still forming stars in the blue cloud, we may then expect the bimodality to actually become stronger, before weakening again as the fraction of those galaxies already on the red sequence becomes small at moderate-to-high redshifts. In general, however, the color distributions shown in Figure 5 are not clearly bimodal.

With this in mind, as a simple means of separating red from blue galaxies, we have fit the observed distributions in each redshift bin with double Gaussian functions. These fits are shown by the smooth curves in each panel of Figure 6. For the most part, these fits provide a reasonable description of the $0.2 < z_{\text{phot}} \lesssim 1.2$ data (see also Borch et al. 2006).

6.2. A Massive Galaxy Red Sequence at $z_{\text{phot}} \gtrsim 1.3$?

In contrast to lower redshifts, for $z_{\text{phot}} \gtrsim 1.3$, we are no longer able to reliably fit the color distributions in this manner: on the basis of the sensitivity tests presented in §9, neither the red/blue separation nor the fits to the distributions of these populations is robust. Looking at the typical errors shown in each panel of Figure 5, the measurement errors on the $(u-r)$ colors of red galaxies rises sharply from $\Delta(u-r) \lesssim 0.1$ mag for $z_{\text{phot}} \lesssim 1.2$ to 0.2 mag for $z_{\text{phot}} \sim 1.3$, 0.3 mag for $z_{\text{phot}} \sim 1.5$, and 0.4 mag for $z_{\text{phot}} \sim 1.7$. This would suggest that our inability to reliably distinguish both a red and a blue population at these higher redshifts may very well be due to the large errors in restframe colors for higher redshift galaxies.

In order to help interpret our $z_{\text{phot}} \gtrsim 1$ results, we have tested our ability to recover a single-color galaxy population, given our observational and analytical errors. To this end, we have generated a mock photometric catalog

containing only red sequence galaxies: beginning with our main galaxy sample, we have replaced each galaxy’s photometry using synthetic spectra for a SSP formed over a short period beginning at $z_{\text{form}} = 5$, assuming the catalog values of z_{phot} and M_* , and then adding typical MUSYC ECDFS photometric errors. We have then re-analyzed this catalog using the same methods and procedures as for the main analysis, including re-computing photometric redshifts, restframe colors, and stellar masses.

The results of these tests are shown in Figure 7, which plots the observed width of the color distribution for this intrinsically single color population, as a function of photometric redshifts, assuming photometric errors typical for the MUSYC ECDFS (squares). The measurement errors on the $(u-r)$ colors of red galaxies rise sharply from 0.05–0.07 mag for $z_{\text{phot}} \lesssim 1$ to 0.10 mag for $z_{\text{phot}} \approx 1$, and then continue to increase for higher redshifts. In order to demonstrate that this is a product of photometric errors *per se* and not redshift errors, we have also repeated this analysis holding the redshifts of each object fixed; the results of this test are shown as the dotted line. Even with spectroscopic redshifts, the depth of our NIR data would seem to preclude the detection of a distinct red sequence at $z \gtrsim 1.3$.

What then would be required in order to confirm the non/existence of a red sequence at $z_{\text{phot}} \gtrsim 1.5$? We have also constructed mock galaxy catalogs with S:N that is 2.5 and 10 times greater than typical values for the MUSYC ECDFS catalog; the results of these tests are shown as the triangles and circles, respectively. Even

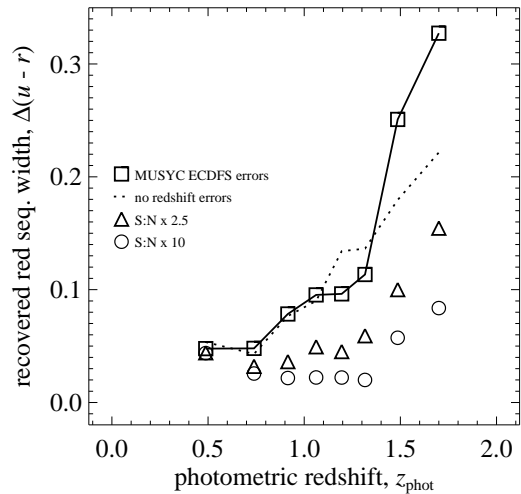


FIG. 7.— The effects of photometric errors on our ability to recover a (red) single-color galaxy population—These results are based on mock galaxy catalogs containing only passively evolving galaxies, taking redshifts and stellar masses of galaxies from the main sample, which we have analyzed in the same manner as the actual data: we are thus testing our ability to recover a single-color galaxy population as a function of redshift. The squares, triangles, and circles show the width of the recovered color distributions assuming typical errors for the MUSYC ECDFS data divided by 1, 2.5, and 10, respectively; the dotted line shows the results assuming MUSYC ECDFS photometric errors, but no redshift errors. Even with spectroscopic redshifts, the depth of the MUSYC ECDFS NIR data precludes the detection of a $z_{\text{phot}} \gtrsim 1.4$ red sequence.

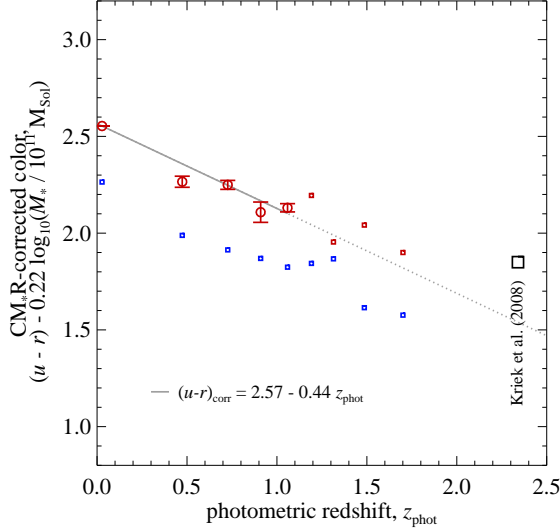


FIG. 8.— The color evolution of massive galaxies for $z \lesssim 2$ — Points show the fit centers of the color distributions for the red and blue galaxy subpopulations (see Figure 6). Only the $z_{\text{phot}} \lesssim 1.2$ points (circles with error bars) were used when fitting for the color evolution of the red galaxy sequence (solid line); the errors were derived from bootstrap resampling. The large square at $z = 2$ shows the approximate equivalent $(u-r)$ color of the 3.3σ detection of a $(U-B)$ red sequence among $z \sim 2$ galaxies from Kriek et al. (2008), based on NIR spectra. We see rather a rather smooth reddening of the red sequence from $z \sim 1.2$ to the present day, which is well described by the linear fit given.

pushing a full magnitude deeper, it would be difficult to identify a red sequence at $z \sim 1.5$, assuming that observational errors of $\Delta(u-r) \lesssim 0.1$ mag would be required to robustly identify a red sequence. In order to probe $z \gtrsim 1.5$, an order of magnitude improvement is required. This would suggest that the detection of a red sequence at $z \gtrsim 1.5$ would require a J band (5σ point source) limit of ~ 25.8 , roughly the final target depth for the Ultra Deep component of the UKIRT Infrared Deep Sky Survey (Lawrence et al. 2007).

It is clear from this analysis that we cannot confirm or exclude the existence of a red galaxy sequence at $z \gtrsim 1.3$ on the basis on the present data. This is in good accord with the recent detections of a $z \lesssim 1.5$ red galaxy sequence by Cirasuolo et al. (2007) and Franzetti et al. (2007 — see also Kriek et al. 2008). Moreover, we note in passing that if we were to subtract away the broadening effect of photometric errors, as derived from the test described above, then the implied intrinsic width of the red sequence is ≈ 0.1 mag for all $z_{\text{phot}} \lesssim 1.2$, consistent with the $z_{\text{spec}} < 1.0$ findings of Ruhland et al. (2008).

7. THE COLOR EVOLUTION OF MASSIVE RED GALAXIES

Our next task is to quantify the color evolution of the massive red galaxy population. We have addressed this question based on the double Gaussian fits to the (CM_{*}R-corrected) color distributions of $M_* > 10^{11} M_\odot$ galaxies shown in Figure 6. In Figure 8, we plot the fit centers of the blue (lower points) and red (upper points) galaxy color distributions as a function of redshift; the errors on the locus of the massive red galaxy population

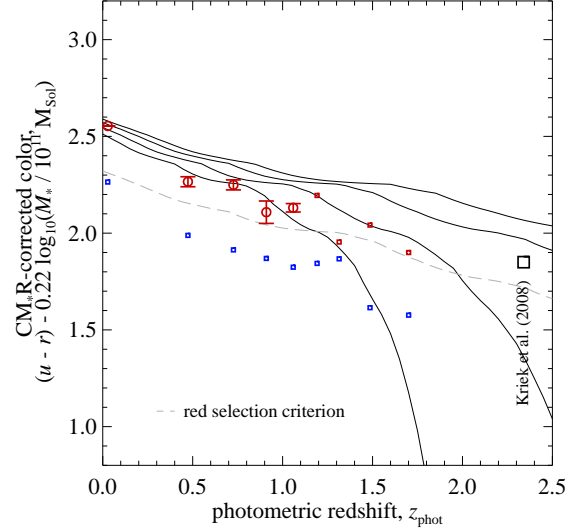


FIG. 9.— Comparing the color evolution of massive galaxies for $z \lesssim 2$ to passively evolving stellar population models — The data in this panel are identical to Figure 8. The overlaid curves show simple expectations for the passive evolution of a SSP, formed in a short burst (e -folding time of 100 Myr) beginning at $z_{\text{form}} = 2, 3, 5$, and 10 (bottom to top). While the $z_{\text{form}} \gtrsim 3$ curves provide a good qualitative description of the observed evolution, they have substantially lower metallicity than would be expected from the local mass-metallicity relation. Moreover, these very simple models make no attempt to account for progenitor bias, and other important effects.

shown in this Figure have been obtained by bootstrap resampling.

From this plot, it is clear that the red galaxy population as a whole has become progressively redder by ~ 0.4 mag in $(u-r)$ over the past 9 Gyr; the evolution in the blue cloud is similar. Making a linear fit to the (robust) $z_{\text{phot}} < 1.1$ measurements, we find $\Delta(u-r)_{\text{corr}} = 2.57 - (0.44 \pm 0.02) z_{\text{phot}}$. (Note that this fit is constrained to match the $z \approx 0$ point.) These results do not change significantly if we also include the point $z_{\text{phot}} \sim 1.2$, but it is clear that if we were to fit to the $z_{\text{phot}} \gtrsim 1.3$ points, we would find slightly less strong evolution.

Kriek et al. (2008) report a 3.3σ detection of a red sequence in the spectrally derived $(U-B)$ color distribution of a mass-selected sample of 36 $z_{\text{phot}} \gtrsim 2$ galaxies, 12 of which lie in the ECDFS. The square at $z = 2$ in Figure 8 shows the approximate $(u-r)$ color equivalent of their red sequence detection. While the Kriek et al. (2008) point is slightly redder than an extrapolation of our linear fit, the two results agree rather well.

In Figure 9, we compare the observed color evolution of the red galaxy population with naïve expectations from passive evolution of synthetic spectra. For this purpose, we have used Pégase V2.0 (Le Borgne & Rocca-Volmerange 2002) models with an initial metallicity of $Z = 0.004$, and assuming a short burst of star formation (e -folding time of 100 Myr), beginning at $z_{\text{form}} = 2, 3, 5$, or 10 (bottom to top).

The $z_{\text{form}} \gtrsim 3$ tracks do an adequate job of describing the amount of observed evolution for $z_{\text{phot}} < 1.3$. However, to get this level of agreement, the model (luminosity

weighted) metallicities at $z = 0$ must be roughly solar ($Z \approx 0.2$), whereas the local mass-metallicity relation would suggest that these abundances should be super-solar by a factor of 3 or more (Tremonti et al. 2004). If we were to adopt $Z = 0.2$ initially, leading to final metallicities that are super-solar by approximately 50 %, the model colors would become nearly 0.5 mag too red. The problem is even worse for SSP models: while solar metallicities lead to colors which are too red by 0.25 mag, an acceptable description of the data is only possible assuming roughly half solar abundances. (See also Bell et al. 2004.)

Nevertheless, these simple models do provide an acceptable description of the rate or amount of color evolution of the red galaxy population, $\Delta(u-r)$, if not the $(u-r)$ colors *per se*. Using these extremely simple models to interpret the color evolution of the red galaxy population, the observations suggest that the bulk of the stars in massive red galaxies were formed at $z \gtrsim 3$; including the point from Kriek et al. (2008) would suggest a formation redshift $\gtrsim 5$.

This is not to say, however, that the observations are consistent with all massive red galaxies being formed at $z \gtrsim 5$, or even 3: even among $M_* > 10^{11} M_\odot$ galaxies, there are simply not enough stars at $z \gtrsim 2$ to build the $z \approx 0$ red sequence population (Fontana et al. 2006; Conselice et al. 2007, see also Figure 10). Instead, what we see is that the colors of massive red galaxies are consistent with being dominated by ancient stars at all redshifts. This implies both extended star formation histories among red galaxies (and/or their progenitors), as well as a large spread in the times at which galaxies of a given (stellar) mass join the red population — a kind of long migration of galaxies, occurring over many Gyr (*cf.* Brown et al. 2008). A proper description of red sequence evolution would therefore have to account for, among other things, progenitor bias (Van Dokkum & Franx 2001): the continual skewing of the population by new additions (see also Faber et al. 2007; Ruhland et al. 2008). This is beyond the scope of this work.

8. THE RISE OF RED GALAXIES OVER $z_{\text{phot}} \lesssim 2$

In this section, we turn our attention to the third of our basic results. Whereas our focus until now has been on the properties of the red galaxy population as a whole, we now look at how the number of red galaxies within the total massive galaxy population—*ie.* the red galaxy fraction—evolves with time.

8.1. Defining a Red Galaxy Selection Criterion

Our inability to robustly distinguish separate red and blue galaxy populations on the basis of the observed color distributions for $z_{\text{phot}} \gtrsim 1.2$ forces us to devise some alternate means of separating ‘red’ galaxies from the general field population.

We have already seen that the color evolution of the red galaxy population is roughly consistent with ancient stars at all redshifts (Figure 9). Our simple solution is therefore to use the predicted color evolution for a passively evolving stellar population formed at high redshift to define a redshift-dependent ‘red’ selection criterion,

viz.:

$$(u-r) > 2.57 + 0.24 \times \log_{10}(M_*/10^{11} M_\odot) + \delta(z_{\text{phot}}) - 0.25, \quad (2)$$

where $\delta(z_{\text{phot}})$ is the $(u-r)$ color evolution of a SSP with $z_{\text{form}} = 5$, as shown in Figure 9. This selection limit is shown as the dashed lines in each of Figures 5, 6, and 8.

How does this definition of ‘red’ relate to things like membership of the red sequence, star formation rate and/or history, etc.? As we remarked in the first paragraph, a galaxy’s optical color is a reflection of its mean stellar age, modulo the complicating factors of metallicity and dust extinction. In addition to ‘red and dead’ galaxies, therefore, simply selecting ‘red’ galaxies can potentially catch a significant number of star forming galaxies with high dust obscuration. In other words, while all passive galaxies are red, not all red galaxies are passive.

In this sense, it is not unreasonable to interpret the redshift evolution of the number and fraction of red, massive galaxies as placing an upper limit on the numbers of ‘fully formed’ (in the sense that they have essentially completed their star formation and/or assembly) massive galaxies. These results can thus be used to constrain the epoch at which the star formation quenching mechanism operates.

8.2. The Number Density Evolution of Massive Galaxies for $z_{\text{phot}} < 1.8$

Figure 10 shows the evolving number density of $M_* > 10^{11} M_\odot$ galaxies for $z_{\text{phot}} < 1.8$. As before, the $z \approx 0$ point comes from our analysis of the low- z sample discussed in Appendix A; the histograms are for the main MUSYC ECDFS sample. For the $z \gg 0$ galaxies, since we have used bins of equal comoving volume, the observed numbers (*right axes*) can be directly related to a comoving number density (*left axes*), modulo uncertainties in the cosmological model. The black point/histograms refer to the total $M_* > 10^{11} M_\odot$ population; the red point/histograms refer to red galaxies only; the dotted lines show where our results are significantly affected by incompleteness.

The error bars on the $z \gg 0$ histograms include the estimated measurement uncertainty due to field-to-field variation, derived as in Somerville et al. (2004), but modified for cuboid rather than spherical volumes (R Somerville, priv. comm.). For any single measurement, this is the dominant source of uncertainty: typically ~ 30 %, as compared to random photometric errors, which are at the ~ 10 % level. Note, however, that each of the $z_{\text{phot}} \gtrsim 1$ bins contains its own ‘spike’ in the z_{spec} distribution (Vanzella et al. 2008); the $0.6 < z_{\text{phot}} < 0.8$ bin contains two, and the $0.8 < z_{\text{phot}} < 1.0$ bin none. Further, note that for $z_{\text{phot}} \gtrsim 1$, our redshift errors are comparable to the size of the bins themselves; in this sense, the densities in neighboring bins are correlated, and the variations due to large scale structure are to a certain extent masked.

The observed evolution in the number density of massive galaxies is moderate: the number density of $M_* > 10^{11} M_\odot$ galaxies at $1.5 < z_{\text{phot}} < 1.8$ is 52 ± 8 % of the $z \approx 0$ value. We see a very similar trend in the mass density, although a handful of galaxies with inferred $M_* \gg 10^{12} M_\odot$ make this measurement considerably noisier.

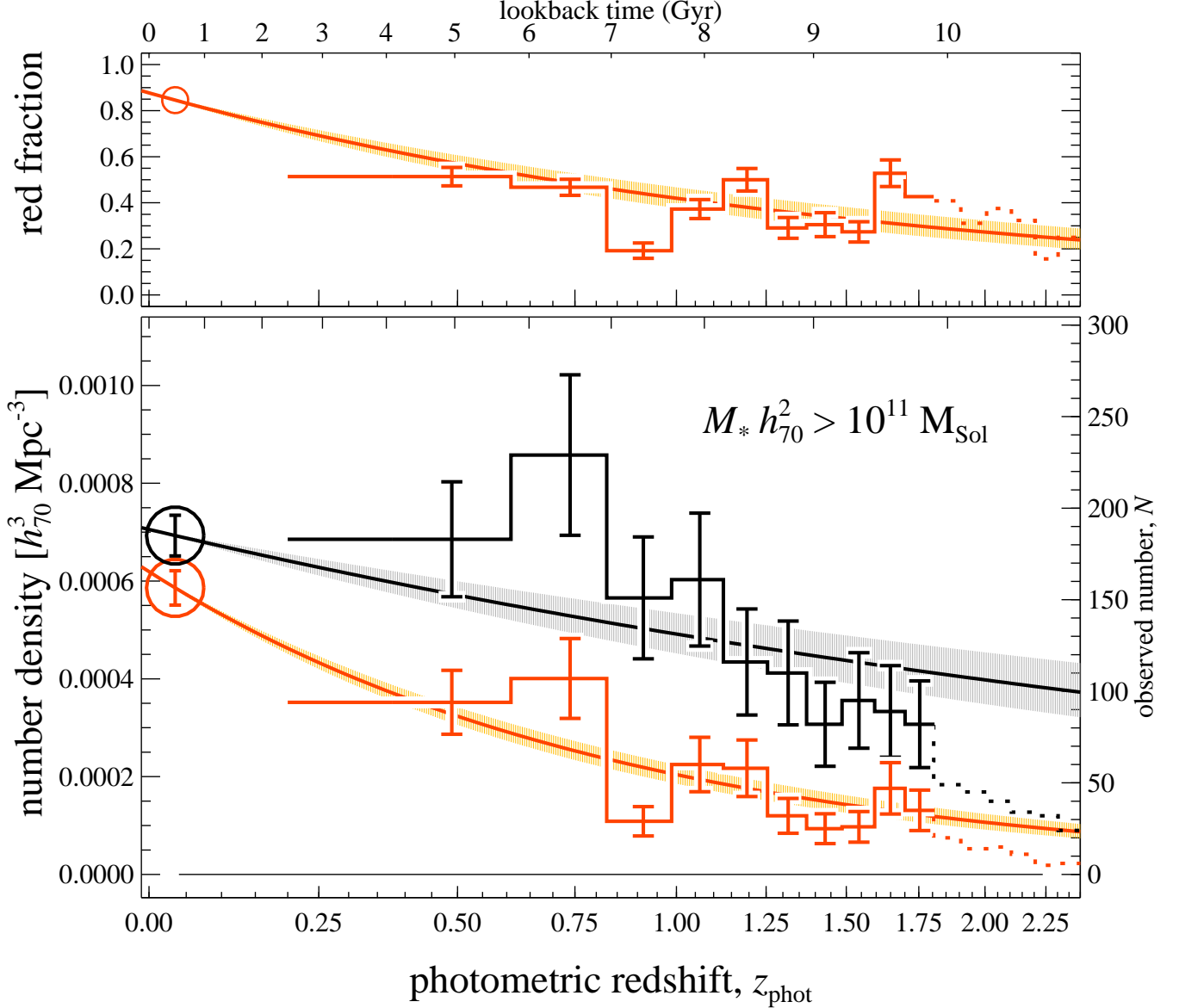


FIG. 10.— The rise of massive, red galaxies over cosmic time—*Lower panel*: evolution in the number density of all galaxies (*black histograms*) and of red galaxies (*red histograms*) with $M_* > 10^{11} M_\odot$ in the MUSYC ECDFS catalog; The error bars shown reflect the expected field-to-field variation, calculated as per Somerville et al. (2004). *Upper panel*: evolution in the red galaxy fraction among $M_* > 10^{11} M_\odot$ galaxies, as a function of photometric redshift. In this panel, the error bars have been derived by bootstrap resampling. In both panels, the dotted histograms show where we are significantly affected by incompleteness. The $z \approx 0$ points (*circles*) are derived from the low- z sample, discussed in Appendix A. The smooth curves show our fits to the observations; the shaded regions show the 1σ uncertainties in the fits: we find $\gamma_{\text{tot}} = -0.52 \pm 0.12$, $\gamma_{\text{red}} = -1.70 \pm 0.14$, and $\gamma_{\text{frac}} = -1.17 \pm 0.18$.

In order to quantify the observed evolution, we have made a parametric fit to our measured number densities of the form:

$$n_{\text{tot}}(z) = n_0 (1+z)^{\gamma_{\text{tot}}} . \quad (3)$$

In practice, since the dominant source of uncertainty in any single point is from field-to-field variance, we perform a linear fit in $\log n - \log(1+z)$ space, weighting each point according to its uncertainty as shown in Figure 10. Further, we constrain the fits to pass through the $z \approx 0$ point, effectively eliminating n_0 as a free parameter. In this way, we find $\gamma_{\text{tot}} = -0.52 \pm 0.12$. The fit itself is shown in Figure 10 as the smooth black curve;

the shaded region shows the 1σ uncertainty in the fit.

8.3. Evolution in the Red Galaxy Fraction from $z_{\text{phot}} = 1.8$ to the Present Day

We now turn our attention to the red galaxy population. From Figure 10, it is clear that the observed evolution is much stronger for red galaxies than it is for the total population: the number density of red galaxies at $1.5 < z_{\text{phot}} < 1.8$ is $18 \pm 3\%$ of the $z \approx 0$ value. Making a fit to the red galaxy number densities to quantify this evolution, in analogy to the previous section, we find $\gamma_{\text{red}} = -1.60 \pm 0.14$ (*smooth red curve*).

A complementary way of characterizing the rise of massive red galaxies is to look at the evolution of the red galaxy fraction. There are several advantages to focusing on the red galaxy fraction, rather than the number density of red galaxies *per se*. First and foremost, the uncertainty in the red fraction due to large scale structure and field-to-field variation should be considerably smaller than those in the number density, especially at $z \gtrsim 1$ (Cooper et al. 2007).

We show the red fraction as a function of photometric redshift in the upper panel of Figure 10. Fitting these results (*smooth red curve*) with the same functional form as in Equation 3, we find $\gamma_{\text{frac}} = -1.06 \pm 0.16$. Taken together, the results encapsulated in Figure 10 suggest that $\lesssim 20\%$ of $M_* > 10^{11} M_\odot$ galaxies in the local universe were already on the red sequence by $z_{\text{phot}} \approx 1.6$ (9.5 Gyr ago). By the same token, approximately 50 % of these galaxies only (re-)joined the red sequence after $z = 0.5$ (5.0 Gyr ago).

8.4. The Importance of the $z \approx 0$ Comparison Point

It is clear from Figure 10 that almost all the signal for $z \gg 0$ evolution in the red fraction comes from the $z \approx 0$ comparison point (see also Borch et al. 2006). Fitting to the $z \gg 0$ data alone, we find $f_{\text{red}} = (0.53 \pm 0.05) (1 + z_{\text{phot}})^{-0.29 \pm 0.17}$; that is, less than a 2σ signal of evolution. The same is also true for the number density measurements (see also Borch et al. 2006); the reasons for this are not just the relatively mild evolution, but also to the relative size of the error bars on the low- and high-redshift measurements. Fitting only to the $z \gg 0$ points, we find $\gamma_{\text{tot}} = -1.55 \pm 0.84$ and $\gamma_{\text{red}} = -1.77 \pm 1.84$; these fits ‘overpredict’ the $z \approx 0$ number densities by factors of 2.2 and 1.3, respectively.

In this sense, then, rather than quantifying the absolute evolution in the $z \gg 0$ population, we are performing a difference measurement between the situations at $z \approx 0$ and $z \gg 0$. For this reason, it is imperative that care is taken when deriving the $z \approx 0$ comparison values to ensure that the low- and high-redshift samples have been analyzed in a uniform way (Appendix A).

In comparison to more sophisticated analyses by Bell et al. (2003) and Cole et al. (2001), both of which combine the 2MASS and SDSS datasets, our $z \approx 0$ number densities are approximately 10 % higher, and 15 % lower, respectively. Adopting these values in place of our own determinations, we find $\gamma_{\text{tot}} = -0.72 \pm 0.12$ using the Bell et al. (2003) mass function, and $\gamma_{\text{tot}} = -0.42 \pm 0.12$ using the Cole et al. (2001) mass function, changes of -0.2 and $+0.1$ with respect to our default analysis. These rather large discrepancies underline the importance of uniformity in the analysis of high- and low-redshift galaxies.

8.5. Comparison with Other Works

In Figure 11, we compare our results to a selection of the steadily growing number of similar measurements; we show results from: the COMBO-17 survey (Borch et al. 2006), the GOODS-MUSIC catalog (Fontana et al. 2006), the K20 survey (Fontana et al. 2004), the VVDS (Pozzetti et al. 2007), the DEEP2 survey (Bundy et al. 2006), and MUNICS (Drory 2004). (Note that all of these results have come within the

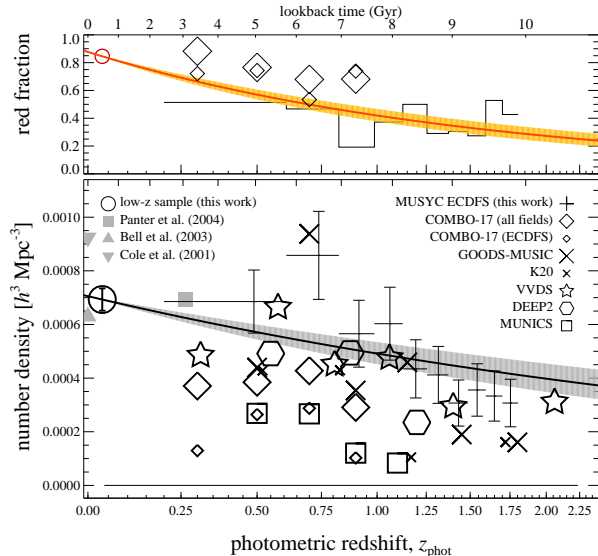


FIG. 11.— Comparison with other works—The different symbols correspond to different authors and surveys as marked: the filled symbols refer to other authors’ analyses of SDSS data; references for other $z \gg 0$ surveys are given in the main text. As in Figure 10, the smooth curves show our fits to the MUSYC ECDFS data; the shaded regions show the 1σ errors on the fits. Excepting the MUSYC ECDFS data points, all points have been derived by integrating up Schechter function fits to the observed mass functions, in redshift bins. Apart from the MUNICS and the COMBO-17 ECDFS data points, there is good agreement between the many different groups’ results; the cause for the discrepancy between the COMBO-17 and MUSYC results in the ECDFS is investigated in Appendix B.

last five years.) In all cases, the points shown in Figure 11 have been obtained by integrating up a fit mass function, taking into account different choices of cosmology and IMF. We note that the strong redshift spike at $z_{\text{phot}} \sim 0.7$ is also present in the GOODS-MUSIC results, which are based on the CDFS.

The comparison with the COMBO-17 results deserves some further comment. While our results agree reasonably well with the combined results from three of the COMBO-17 fields (*large diamonds*), there is significant disagreement between our results and the COMBO-17 results in the ECDFS (*small diamonds*). In Appendix B, we present a detailed comparison between the MUSYC and COMBO-17 datasets, and demonstrate that the discrepancy between the two results is due to systematic calibration errors in the COMBO-17 photometry, rather than differences in our analyses. We note in passing that these calibration errors have only a small effect on the COMBO-17 photometric redshifts, and affect the ECDFS only; not the other COMBO-17 fields (Wolf et al. 2008).

Particularly given the significant uncertainties in these measurements, and with the possible exception of the MUNICS results, the degree of agreement between these surveys is impressive. However, in all of these surveys, field-to-field variance is a—if not the—major source of uncertainty. More and larger fields are necessary to lock down the growth rate of massive galaxies.

9. QUANTIFYING POTENTIAL SYSTEMATIC ERRORS

Having now described our experiment in full, in this section we describe a wide array of sensitivity analyses, in order to determine how sensitively our results depend on specific choices in our experimental design. The basic idea is to vary individual aspects of our analysis, and see what effects these changes have on the results presented in §8; in particular, we will focus on how the best-fit values of γ_{tot} and γ_{frac} depend on our experimental design. The results of many of these tests are summarized in Tables 2 and 3. Note that we have used the same red galaxy selection criterion (Equation 2) throughout all of these tests.

We will consider, in turn, how sensitive or robust our results are to basic photometric calibration errors (§9.1), the methods used for the photometry itself (§9.2), incompleteness (§9.3), and variations on our photometric redshift computation (§9.4). We then discuss possible systematic effects arising from our method for estimating stellar masses in §9.5, and other concerns in §9.6. Our findings in the section are summarized in §9.7.

9.1. Photometric Calibration

How sensitive or robust are our results to errors in the basic photometric calibration? And how accurate are the calibrations of each of the different bands, relative to one another, and in an absolute sense? We address these two questions in this section.

9.1.1. The Effect of Perturbing Individual Bands

In order to gauge the effect of calibration errors on our final results, we have perturbed the photometry in each band in turn by ± 0.05 mag, and repeated our full analysis, from the derivation of photometric redshifts and stellar masses to fitting the γ s. Roughly speaking, these perturbations can affect our results in two separate ways: either through direct changes in the SEDs themselves, or indirectly, through changes in the derived photometric redshifts, and so the transformation from observed to restframe quantities. In order to disentangle these two effects, we have also repeated our analysis with these ± 0.05 mag shifts, but while holding the photometric redshifts fixed to their default values. The results of these tests are summarized in Table 2.

For the UBV bands, the effect of changing the photometric calibration on our main results is driven almost exclusively by changes in the photometric redshifts. This is simply because our stellar mass estimates typically do not depend directly on the observed UBV photometry: the restframe B has already shifted past the observed V by $z \approx 0.25$. (Recall that we use the $B - V$ color to infer M_*/L_V , and thus M_* .) Similarly, the effect that changing the reddest H and K bands has on γ_{tot} is small: $\pm < 0.02$ for both. The situation changes for the $RIzJ$ bands, where the direct effect comes to dominate over the indirect effect from changes in the redshifts.

In terms of the SED photometry, our results are most sensitive to errors in the R and J band photometric calibrations: a ± 0.05 mag shift in the R or J zeropoint changes the value of γ_{tot} by ∓ 0.08 or ± 0.14 , respectively. For the R band, the effect on restframe properties is focused on the $z_{\text{phot}} \approx 0.7$ bin, where we happen to measure the highest density; this is also the $z \gg 0$ bin that has the single greatest effect on our measurement of γ_{tot} . The critical importance of the J band stems from the

fact that it plays a role in the derivation of restframe V photometry, and thus M_* , for all $z_{\text{phot}} \gtrsim 1$; *ie.*, roughly two thirds of our surveyed volume. It seems plausible that our sensitivity in this regard might be substantially reduced if we were to use a different method for estimating stellar masses (see also §9.5).

While the SED modeling results are not particularly sensitive to the K band calibration, it still plays a critical role in normalizing each SED through the total K flux measurement. Although changing the K calibration by ± 0.05 mag effectively rescales the stellar masses by just ∓ 0.02 dex, this can change the inferred number densities by as much as ∓ 10 %. In terms of γ_{tot} , the effect is ∓ 0.07 .

9.1.2. Testing the MUSYC ECDFS Photometric Calibration

We now turn our attention to identifying and quantifying potential calibration errors in the MUSYC ECDFS dataset. We will then be able to use this information to estimate the extent to which our results may actually be affected by such errors.

To address this question, we have used EAZY to fit main sequence stellar spectra from the BPGS stellar atlas (Gunn & Stryker 1983), fixing $z_{\text{phot}} = 0$, to the observed photometry for stars. Assuming that whatever calibration errors do exist do not affect the choice for the best fit template spectrum, we can then interpret the mean difference between the best fit and the observed photometry as being the product of calibration errors. We note that since this test is concerned exclusively with SED shapes, it cannot comment on the absolute calibration of any given band; instead it assesses the relative- or cross-calibration of the ten band photometry that makes up the MUSYC ECDFS dataset.

The offsets we derive in this way are given in Col. (10) of Table 2. The most notable offsets derived in this way are -0.048 in $(U - U_{38})$, 0.033 in $(I - z')$, 0.064 in $(J - H)$, and 0.032 in $(J - K)$. These offsets give an indication of the plausible size of any calibration errors or inconsistencies in the MUSYC SED photometry. If we recalibrate our photometry to eliminate these apparent offsets (holding the K band fixed), and repeat our full analysis, we find that the best fit values of γ_{tot} , γ_{red} , and γ_{frac} change by $+0.00$, $+0.02$, and $+0.04$, respectively.

We have also checked the absolute calibration of each band in comparison to the FIREWORKS catalog (Wuyts et al. 2008) in the region of overlap (Paper I). Using $(B - z') - (z' - K)$ selected stars, we have constructed empirical ‘color transforms’ between FIREWORKS and MUSYC filters, as a function of HST color. Comparing these diagrams to predictions derived from the BPGS stellar spectral atlas (Gunn & Stryker 1983), we treat any offset between the predicted and observed stellar sequences as a calibration error in the MUSYC photometry. (This is the same method we used to identify the disagreement between the COMBO-17 and MUSYC calibrations discussed in Appendix B.)

The offsets we have derived in this way are given in Col. (11) of Table 2. The biggest offsets derived in this way are ≈ 0.05 mag in $(B - F435W)$ and $(I - F850LP)$. The offset in $(K - K_{\text{ISAAC}})$ is -0.017 mag; for the crucial J band, the offset is just $+0.015$ mag. In agreement with

TABLE 2
PHOTOMETRIC CALIBRATION SENSITIVITY TESTS

Band	z_{phot} fixed		change in γ_{tot}		Recalculating z_{phot}		change in γ_{red}		change in γ_{frac}		Photometric offset with respect to:	
	+0.05 mag	-0.05 mag	+0.05 mag	-0.05 mag	+0.05 mag	-0.05 mag	+0.05 mag	-0.05 mag	+0.05 mag	-0.05 mag	stellar SEDs	FIREWORKS
(1)	(2)	(3)	(4)	(5)	(6)	(7)	(8)	(9)	(10)	(11)		
U	+0.00	+0.00	+0.01	-0.01	+0.02	+0.02	+0.001	+0.041	-0.004	+0.013		
U_{38}	+0.00	+0.00	+0.00	+0.01	+0.01	+0.02	-0.002	+0.009	-0.051	-0.020		
B	+0.00	+0.00	+0.00	+0.00	+0.03	+0.01	+0.061	-0.006	-0.017	+0.050		
V	+0.01	+0.00	-0.02	+0.00	+0.04	-0.10	+0.037	-0.068	-0.006	+0.038		
R	+0.05	-0.03	+0.08	-0.08	+0.06	-0.05	+0.071	-0.053	+0.017	+0.016		
I	+0.04	-0.03	+0.01	-0.02	+0.03	-0.03	-0.051	+0.066	+0.023	+0.055		
z'	-0.02	+0.01	-0.03	+0.02	-0.01	-0.01	-0.011	-0.024	-0.011	-0.004		
J	-0.10	+0.09	-0.13	+0.10	-0.14	+0.11	+0.022	-0.033	+0.032	+0.015		
H	-0.03	+0.03	-0.02	+0.01	-0.02	+0.05	-0.009	+0.039	-0.032	-0.012		
K_{SED}	+0.00	+0.02	-0.02	+0.01	-0.07	+0.08	-0.078	+0.096	—	—		
K_{tot}	-0.07	+0.07	-0.07	+0.07	-0.03	+0.03	+0.057	-0.025	—	-0.017		

NOTE. — For each band (Col. 1), Col.s (2)–(9) give how our parametric fits to the $z_{\text{phot}} \lesssim 2$ evolution of the $M_* > 10^{11} M_{\odot}$ population changes with ± 0.05 mag perturbations to individual bands' zeropoints: Col.s (2) and (3) show the effect on the total number density evolution of massive galaxies due to the change in the photometry only. Col.s (4) and (5) show the same information, but including the effect of changes in the photometric redshifts that come with changing the calibration; similarly, Col.s (6) and (7) show the effect on the number density measurements for red, massive galaxies, and Col.s (8) and (9) show the effect on the red galaxy fraction. Col.s (10) and (11) give zeropoint offsets for each band based on stellar colors and comparison with the FIREWORKS catalogue (Wuyts et al. 2008), respectively.

the stellar SED fitting test, this analysis also finds an inconsistency between the I and z bands at the level of 0.05 mag. If we recalibrate our photometry to match the FIREWORKS catalog, we find that our values of γ_{tot} , γ_{red} , and γ_{frac} change by -0.03 , -0.13 , and -0.08 with respect to our default results. The sizes of these changes are in excellent agreement with the results of the previous section; more than half of these changes can be ascribed just to the 0.02 mag rescaling of total K magnitudes.

We estimate that the systematic uncertainty in our main results due to photometric calibration errors is at the level of $\Delta\gamma_{\text{tot}} \lesssim 0.05$ and $\Delta\gamma_{\text{frac}} \sim 0.10$.

9.2. Photometric Methods

While we rely on SExtractor for our basic photometry, we have introduced three sophistications in our analysis. In this section, we investigate the effects that these three changes have on our results.

9.2.1. Background Subtraction

We have applied a correction to account for the tendency of SExtractor to overestimate the background level; for individual objects, this correction is typically on the order of -0.03 mag. To test the sensitivity of our results to background subtraction errors, we have repeated our analysis without applying this correction. Repeating our analysis relying on our own background estimation we find changes in γ_{tot} and γ_{red} of -0.06 and -0.05 , respectively; the change in γ_{frac} is just -0.02 .

9.2.2. Total Magnitudes

Our total flux measurements are based on SExtractor's AUTO flux measurement. It is well known that the AUTO aperture misses a significant amount of flux, especially for the faintest sources (Bertin & Arnouts 1996; Labbé et al. 2003; Brown et al. 2007). Following Labbé et al. (2003), we partially redress this by applying

a minimal correction to correct for light laying beyond the AUTO aperture, treating each object as if it were a point source. For individual sources, this correction amounts to as much as 20 %. Experiments with synthetic $r^{1/4}$ sources placed in our own image suggest that for the specific example of a $K = 22$ elliptical galaxies with $R_e = 0''.4$ (≈ 3 kpc at $z = 1$), this correction reduces the missed flux from 0.33 mag to 0.15 mag.

In terms of the measured number densities, the effect of adopting this correction is 1–5 % for $z_{\text{phot}} \lesssim 1.5$, rising to 5–10 % for $1.5 < z_{\text{phot}} < 1.8$. The use of uncorrected AUTO fluxes as total flux measurements thus produces a rather mild spurious evolutionary signal. Repeating our analysis without this correction, we find slightly steeper evolution in the number densities: the values of γ_{tot} , γ_{red} change by -0.07 and -0.06 , respectively. By comparison, the red fraction measurements remain almost unchanged: γ_{frac} changes by -0.01 .

9.2.3. SED Apertures and Colour Gradients

When constructing multi-color SEDs, we have used the larger of SExtractor's ISO aperture (based on the $1''.0$ FWHM K mosaic) and a fixed $2''.5$ diameter aperture. This aperture flexibility is intended to guard against potential biases due to color gradients in individual galaxies. This problem is presumably the most severe for the largest, relatively low redshift galaxies with significant bulge components, leading to overestimates in both $(B - V)$ and M_* .

Consistent with this expectation, when repeating our analysis relying exclusively on the fixed $2''.5$ aperture fluxes to construct SEDs, we find the measured number densities of massive galaxies increases by ~ 5 % for $z_{\text{phot}} < 1.1$. The increases in these low redshift bins brings them closer to the $z \sim 0$ point, leading to a slight decrease in the measured evolution: γ_{tot} and γ_{red} change by $+0.05$ and $+0.13$, respectively; γ_{frac} changes by just $+0.02$.

We estimate that the systematic uncertainty in our results associated with our photometric methods are on the order of $\gamma_{\text{tot}} \lesssim 0.07$ and $\gamma_{\text{frac}} \approx 0.00$.

9.3. Correcting for Incompleteness

In §4, we have argued that we are approximately complete for $M_* > 10^{11} M_\odot$ galaxies for $z_{\text{phot}} < 1.8$. In this section, we examine the effects of incompleteness due to both the $K < 22$ detection threshold and the $K \text{ S:N} > 5$ ‘analysis’ selection, by deriving simple completeness corrections.

9.3.1. Incompleteness Due to Low S:N

In addition to incompleteness due to our $K < 22$ detection limit, discussed below, there is the concern of incompleteness due to the $K \text{ S:N} > 5$ selection limit, which we have imposed to ensure against extremely poorly constrained photometric redshifts. This cut affects 4.5 % of all $K \leq 22$ sources in the ECDFS catalog, with 43 % of those galaxies laying in the slightly shallower Eastern pointing. At a fixed magnitude, there is not a strong dependence of the fraction of $\text{S:N} < 5$ detections as a function of $J - K$ color or—with the caveat that this cut is designed to remove poorly constrained redshifts—as a function of z_{phot} .

In order to assess the impact of this cut on our results, in this section we attempt to correct for this additional source of incompleteness. Our procedure is as follows: we determine the completeness fraction in the face of this selection, as function of total K magnitude, $f(K)$; this can then be used to weight each retained galaxy according to its K magnitude, $w(K) = 1/f(K)$. Of galaxies in our main sample, 8 % of all galaxies, and 11 % of $M_* > 10^{11} M_\odot$ galaxies at $1 \leq z_{\text{phot}} \leq 2$ are given $w(K) > 1.25$.

Recalculating our number density measurements using these weights, we find that the number density of massive galaxies at $1.2 < z_{\text{phot}} < 1.8$ changes by less than 5 %; the same is true for red galaxies alone. Repeating our analysis with these corrections, we find $\gamma_{\text{tot}} = -0.49$, $\gamma_{\text{red}} = -1.56$, and $\gamma_{\text{frac}} = -1.05$, amounting to differences of +0.03, +0.04, and +0.01 with respect to our fiducial analysis. We get similar results adopting a more stringent $\text{S:N} > 10$ criterion. To put this change into perspective, it is comparable to that due to uncertainty in the background subtraction for our basic photometry.

9.3.2. Correcting for Undetected Sources

We have corrected for incompleteness due to our $K < 22$ detection limit as follows: taking the $M_* > 10^{11} M_\odot$ galaxy population in a given redshift bin, we then predict what the observed K magnitude for each galaxy would be if the galaxy were shifted through the next most distant redshift bin. In other words, we effectively ‘K correct’ each galaxy’s observed K flux from its fiducial z_{phot} to higher redshifts, using the same machinery as for the interpolation of restframe fluxes. This makes it possible to determine the fraction (in terms of volume) of the next redshift bin over which a given galaxy would remain detectable; the overall completeness is then simply the average of this quantity for all galaxies in the bin. We have performed this correction for red and blue galaxies separately.

Based on this analysis, we are indeed 100 % complete for $z_{\text{phot}} < 1.25$; for $1.7 < z_{\text{phot}} < 1.8$, we are more

than 80 % complete overall, and at least 75 % complete for red galaxies. This agrees reasonably well with our completeness estimates in §4. For higher redshifts, our estimated completeness drops to 75 % for $1.9 < z_{\text{phot}} < 2.0$, and to 65 % for $2.1 < z_{\text{phot}} < 2.2$. The estimated incompleteness correction factor to the measured number densities is thus less than 1.5 for all $z_{\text{phot}} < 2.2$. Using these completeness corrections to extend our analysis to $z_{\text{phot}} < 2.2$, we find $\gamma_{\text{tot}} = -0.47$ and $\gamma_{\text{frac}} = -0.90$; changes of -0.05 and -0.16 with respect to our default values for $z_{\text{phot}} < 1.8$.

Fitting to these incompleteness-corrected measurements for the number density of massive galaxies with $z_{\text{phot}} < 1.8$ (*ie.*, repeating our default analysis, but with a completeness correction), we find $\gamma_{\text{tot}} = -0.37$, -1.42 , and $\gamma_{\text{frac}} = -1.06$. In comparison to our uncorrected results for $z_{\text{phot}} < 1.8$, these represent changes of -0.15 , -0.18 , and $-0.00(3)$, respectively. However, we also note that if we were to assume that we are 100 % complete for $z_{\text{phot}} < 1.4$, these changes become -0.10 , -0.12 , and $+0.01$; that is, the uncertainties on these incompleteness corrections are comparable to in size to the corrections themselves.

9.4. Photometric Redshifts

The next major aspect of our analysis that we will explore in detail is systematic effects associated with the derivation of photometric redshifts; we split this discussion into two parts. In the first part part (§9.4.1) we explore how our results depend on the choice of templates used in the z_{phot} calculation. Then, in the second (§9.4.2), we investigate how our results depend on the exact method used for deriving photometric redshifts, by varying individual aspects of the EAZY algorithm. Some illustrative results from a selection of these sensitivity tests are given in Figure 12.

9.4.1. Trialing Different Template Sets

Using the Fontana et al. (2006) template set—Using a library of ~ 3000 synthetic Pégase V2.0 (Le Borgne & Rocca-Volmerange 2002) spectra described by Fontana et al. (2006), Grazian et al. (2006) obtain $\sigma_z \approx 0.045$ for K selected galaxies from their catalog of the GOODS-CDFS data. In fact, this library provides the parent catalog for EAZY’s default template set (see Brammer et al. 2008). If we use this template library in place of the EAZY default, and do not allow template combination, we find $\sigma_z = 0.039$; the fraction of objects having $\Delta z/(1+z) > 0.1$, $f_{0.1}$, is 16 % (*cf.* 12.4 % for our default redshifts). Adopting these redshifts in place of our default determinations, we find $\gamma_{\text{tot}} = -0.55$ and $\gamma_{\text{frac}} = -1.00$; differences of -0.03 and -0.06 , respectively (see Figure 12).

Using the Rudnick et al. (2003) template set—In the past, our group has tended to determine photometric redshifts as per Rudnick et al. (2003), which considers linear combinations among: four empirical template spectra from Coleman, Wu & Weedman (1980); two starburst spectra from Kinney et al. (1996); and two Bruzual & Charlot (2003) synthetic spectra for SSPs with ages of 10 Myr and 1 Gyr. If we use these templates with EAZY, we find $\sigma_z = 0.055$, with $f_{0.1} = 27$ %. Looking at Figure 12, these photometric redshift determinations suffer from a number of systematics whereby there

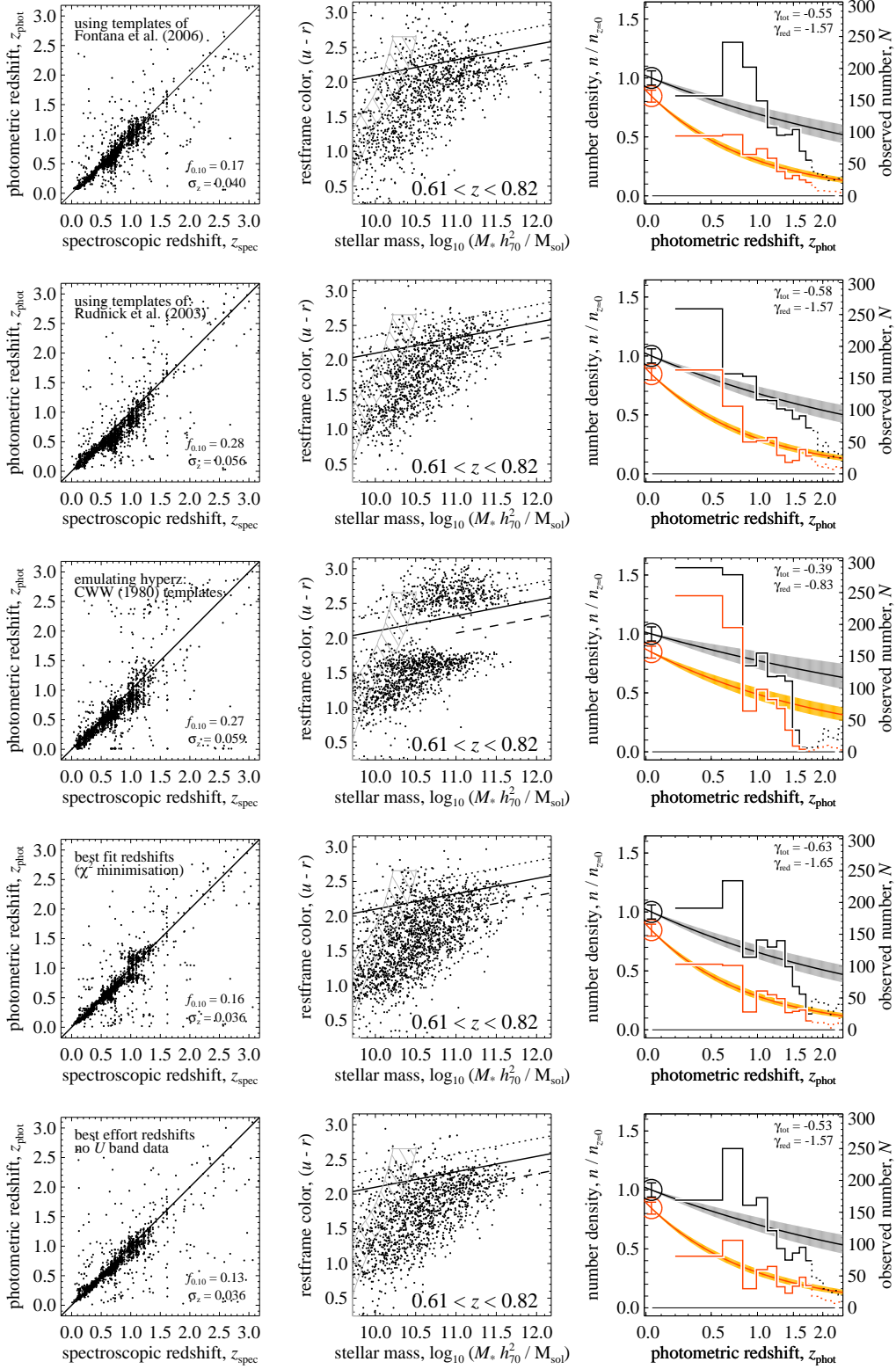


FIG. 12.— The effect of different photometric redshift analyses on our results—In rows, we show how our results would change (*top to bottom*): adopting the template set used by Rudnick et al. (2003); adopting the template set described by ?; emulating hyperz in its default configuration; adopting the maximum likelihood (*ie.* χ^2 minimisation) photometric redshift value; neglecting the U band photometry. In each row, we show (*left to right*) the analogues of Figure 1, the third panel of Figure 5, and Figure 10.

are clear preferred redshift solutions at, *e.g.*, $z_{\text{phot}} \sim 0.4$, as well as a larger systematic underestimate of the true redshift: in addition to the larger random error, we also find a systematic offset in $\Delta z/(1+z)$ of -0.054 . The effect this has on the $z_{\text{phot}} \lesssim 0.8$ number densities is strong, and is dominated by the shifting of many of the galaxies from the $0.6 \lesssim z_{\text{phot}} \lesssim 0.8$ bin down into the $0.2 \lesssim z_{\text{phot}} \lesssim 0.6$ bin. The net effect of this change on our final results is considerably less, however: using these redshifts, we find $\gamma_{\text{tot}} = -0.58$ and $\gamma_{\text{frac}} = -1.11$; changes of -0.06 and -0.05 with respect to our fiducial results.

Emulating hyperz with empirical templates—As a final test for this section, we have also repeated our photometric redshift analysis emulating the popular hyperz (Bolzonella, Miralles & Pello 2000) code in its default configuration; that is, χ^2 minimization between the observed photometry and synthetic photometry using four Coleman, Wu & Weedman (1980) empirical template spectra, and making no allowance for dust extinction beyond what is included in the empirical spectra. Using the spectroscopic redshift sample shown in Figure 1, we find $\sigma_z = 0.060$, and again a substantial systematic offset: $\Delta z/(1+z) = -0.051$.

One very striking consequence of using so few template spectra is a very pronounced biasing of galaxy restframe colors, corresponding to the colors of the template spectra themselves (see Figure 12). This of course has a very strong effect on our stellar mass estimates. For this reason, it is critical when relying on photometric redshifts to derive restframe properties to use a template basis set that spans the full range of galaxy colors.

9.4.2. Variations in our Default Photometric Redshift Calculation

Adopting the best fit redshift—By default, EAZY assigns each object a redshift by taking a probability weighted integral over the full redshift grid. However, it also outputs the single most likely redshift, determined by χ^2 minimization. For these redshifts, we find $\sigma_z = 0.035$, and $f_{0.1} = 14.7\%$. For $1 < z_{\text{spec}} < 2$, however, we find $\sigma_z = 0.086$. We also see evidence for rather strong systematic effects in the photometric redshifts, such that there are preferred photometric redshift solutions, for example at $z_{\text{phot}} \sim 0.8$ and 1.2 (see Figure 12), corresponding to the points where the optical breaks fall between the observed filters. With these redshifts, the values of γ_{tot} , γ_{red} , and γ_{frac} change by -0.11 , -0.05 , and -0.14 , respectively.

No Luminosity Prior—Our default analysis makes use of a Bayesian K band luminosity prior. If we do not include this feature, we find $\sigma_z = 0.038$ and $f_{0.1} = 13.5\%$. The best fit values of γ_{tot} , γ_{red} , and γ_{frac} change by -0.11 , -0.38 , and -0.54 , respectively. These changes are large; however, we note that these results are not internally consistent, in that it is not true that $\gamma_{\text{frac}} \approx \gamma_{\text{red}}/\gamma_{\text{tot}}$. Further, these results are not consistent with the test we describe in §10.

No Template Error Function—A novel feature of the EAZY code is the inclusion of a template error function; *ie.* a systematic error, as a function of restframe wavelength, designed to down-weight those parts of the spectra like the restframe near-UV where galaxies show an greater intrinsic variation. If we do not include this

feature, we find $\sigma_z = 0.034$, and $f_{0.1} = 15.3\%$; the best fit values of γ_{tot} , γ_{frac} , and γ_{frac} change by -0.04 , -0.14 , and -0.13 , respectively.

Two Template Combination—By default, we allow non-negative combinations of all six EAZY templates when fitting to the observed SEDs to determine the redshift. If we instead allow combinations of only two (but any two) of the template spectra, we find $\sigma_z = 0.038$ and $f_{0.1} = 14.4\%$. The fit values of γ_{tot} and γ_{frac} change by $+0.02$ and -0.02 , respectively.

‘Best Effort’ Photometric Redshifts—It is well known that the WFI U filter suffers from a red leak beyond 8000 \AA . We find that we get our best $z_{\text{phot}}-z_{\text{spec}}$ agreement if we ignore the U band photometry in the computation of photometric redshifts. For the spectroscopic sample shown in Figures 1 and 2, we find $\sigma_z = 0.035$ and $f_{0.1} = 12.0\%$; this translates into an uncertainty in the stellar mass estimates due to redshift uncertainties of just 0.1 dex. This only modest improvement in our photometric redshift estimates changes the fit values of γ_{tot} and γ_{frac} change by -0.01 and $+0.05$, respectively.

These tests show that our results do depend rather sensitively on the details of the photometric redshift calculation, typically at the level of $\Delta\gamma \lesssim 0.15$. In particular, the inclusion of a luminosity prior is crucial in shaping our results. However, we note that in most cases there are objective reasons to favor our default redshifts and/or results. Similarly, the use of different template sets changes our results at the level of $\Delta\gamma \approx 0.06$. The effect of minor refinements to our photometric redshift calculation (two template combination versus unrestricted; the inclusion/omission of the U band data) is small: $\Delta\gamma \lesssim 0.05$. Note that, in any case, changing the photometric redshift calculation cannot change our qualitative results: a gradual increase in the red galaxy fraction with time.

9.5. Stellar Mass Estimates

We have relied on a rather simple method for estimating stellar mass-to-light ratios, based on restframe $(B-V)$ colors. Certainly this method does not make use of the full amount of information available in the full, ten-band SED; on the other hand, it does ensure that the same information is used for all galaxies, irrespective of redshift.

Nevertheless, we have trialed reanalyzing our data using standard population synthesis SED fitting techniques to estimate stellar masses for our main sample, in order to assess the potential scale of biases arising from this aspect of our experimental design. Specifically, we have fit Bruzual & Charlot (2003) synthetic spectra to the observed photometry, with redshifts fixed to the fiducial z_{phot} , using the hyperzspec utility, which is a part of the hyperz v1.2 release package (M Bolzonella, priv. comm.).

While the random scatter in comparison to the color-derived stellar mass estimates is 0.18 dex, after correcting for IMF, cosmology, etc., the SED-fit masses are systematically lower by 0.3 dex. This is also true for both the FIREWORKS (Wuyts et al. 2008) or GOODS-MUSIC (Grazian et al. 2006) catalogs of the CDFS-GOODS data. Besides this offset, we do not see evidence for strong evolution in the normalization of the color relation in comparison to the SED fit masses (but

TABLE 3
SUMMARY OF SENSITIVITY TEST RESULTS

Test description (1)	$1.5 < z_{\text{phot}} < 1.8$		$z_{\text{phot}} < 1.8$			$z \approx 2$	
	n_{tot}/n_0 (2)	n_{red}/n_0 (3)	γ_{tot} (4)	γ_{red} (5)	γ_{frac} (6)	n_{tot}/n_0 (7)	n_{red}/n_0 (8)
<i>Fiducial Results</i>							
Default analysis ($z_{\text{phot}} < 1.8$)	0.52 ± 0.08	0.18 ± 0.03	-0.52 ± 0.12	-1.60 ± 0.14	-1.06 ± 0.16	0.57	0.15
Correcting for incompleteness ($z_{\text{phot}} < 2.2$)	0.57	0.20	-0.47 ± 0.09	-1.39 ± 0.10	-0.90 ± 0.11	0.61	0.19
<i>Photometric Calibration</i> (§9.1.2)							
Recalibration to match stellar SEDs	0.54	0.18	-0.52 ± 0.12	-1.58 ± 0.14	-1.02 ± 0.17	0.58	0.16
Recalibration to match FIREWORKS ^(*)	0.49	0.15	-0.55 ± 0.12	-1.73 ± 0.14	-1.14 ± 0.15	0.56	0.13
<i>Photometric Methods</i> (§9.2)							
No correction for background oversubtraction	0.49	0.16	-0.58 ± 0.12	-1.65 ± 0.14	-1.08 ± 0.17	0.54	0.15
No correction for missed flux	0.49	0.16	-0.59 ± 0.12	-1.66 ± 0.14	-1.07 ± 0.17	0.53	0.14
Fixed 2''5 apertures for SEDs	0.52	0.17	-0.47 ± 0.12	-1.47 ± 0.14	-1.04 ± 0.14	0.61	0.18
<i>Incompleteness Corrections</i> (§9.3)							
Correcting for incompleteness ($z_{\text{phot}} < 1.8$)	0.57	0.20	-0.37 ± 0.12	-1.42 ± 0.13	-1.06 ± 0.15	0.67	0.19
Correcting for K S:N < 5 incompleteness	0.54	0.18	-0.49 ± 0.12	-1.56 ± 0.14	-1.05 ± 0.16	0.59	0.16
<i>Using Other z_{phot} Template Sets</i> (§9.4.1)							
Using Rudnick et al. (2003) templates	0.52	0.14	-0.58 ± 0.12	-1.57 ± 0.14	-1.11 ± 0.15	0.54	0.16
Using Fontana et al. (2006) templates ^(*)	0.53	0.21	-0.55 ± 0.12	-1.57 ± 0.14	-1.00 ± 0.09	0.56	0.16
Emulating hyperz with CWW (1980) templates	0.48	0.24	-0.39 ± 0.14	-0.83 ± 0.15	-0.69 ± 0.15	0.66	0.35
<i>Variations on our Default z_{phot} Analysis</i> (§9.4.2)							
Adopting the best fit redshift	0.55	0.22	-0.63 ± 0.13	-1.65 ± 0.14	-0.92 ± 0.14	0.51	0.15
No K luminosity prior	0.41	0.09	-0.63 ± 0.12	-1.98 ± 0.15	-1.59 ± 0.22	0.51	0.10
No template error function	0.53	0.15	-0.56 ± 0.12	-1.74 ± 0.14	-1.19 ± 0.20	0.55	0.13
Two template combinations	0.54	0.16	-0.50 ± 0.12	-1.56 ± 0.14	-1.08 ± 0.15	0.59	0.16
Neglecting U data ('best effort' $z_{\text{phot}}S$)	0.46	0.19	-0.53 ± 0.12	-1.59 ± 0.14	-1.01 ± 0.16	0.57	0.16
<i>Other Variations</i> (§9.5 and §9.6)							
SED-fit stellar masses	0.48	0.19	-0.49 ± 0.12	-1.62 ± 0.14	-1.11 ± 0.14	0.59	0.15
Including spectroscopic redshifts	0.51	0.18	-0.54 ± 0.12	-1.60 ± 0.14	-1.06 ± 0.14	0.56	0.15
Excluding X-ray detections	0.50	0.18	-0.59 ± 0.12	-1.63 ± 0.14	-1.03 ± 0.15	0.53	0.15
GOODS area only	0.47	0.22	-0.63 ± 0.17	-1.37 ± 0.24	-1.00 ± 0.25	0.51	0.20

NOTE. — Each row describes a different sensitivity test, designed to determine how and how much our main results depend on our choice of experimental design. These tests are described in §9. Each row gives an identifier (Col. 1), a different test; references are given for a description of each. For the 'Dissecting our Default z_{phot} Analysis' tests, additional z_{phot} information is given in §9.4.2. For each test, we give the measured number density of $M_* > 10^{11} M_\odot$ galaxies with $1.5 < z_{\text{phot}} < 1.8$: these values are given for the total massive galaxy samples (Col. 2), and the red subpopulation (Col. 3), and are normalised relative to the $z \approx 0$ value for all galaxies. We also give the best fit values for the total $0.2 < z_{\text{phot}} < 1.8$ evolution in the number density of all massive galaxies (Col. 4), in the number density of red, massive galaxies (Col. 5), and in the red fraction among massive galaxies (Col. 6). Finally, we give values for the number density of massive galaxies (Col. 7) and of red, massive galaxies (Col. 8), obtained by extrapolating the fits to $z = 2$. Dominant effects are marked with an asterisk; a summary of our interpretations of these results can be found in §9.7.

see Lin et al. 2007). Since we have not been able to identify the source of this offset, we have simply corrected for it. Note, however, that we have not refit the $z \approx 0$ SEDs for this test.

Using these SED-fit stellar masses, we find $\gamma_{\text{tot}} = -0.49$, $\gamma_{\text{red}} = -1.62$, and $\gamma_{\text{frac}} = -1.11$. These represent differences of just +0.03, -0.02, and -0.05 with respect to our fiducial values. Similarly, using the prescription for M/L as a function of $(B-V)$ from Bell et al. (2003) rather than that from Bell & de Jong (2001), we find $\gamma_{\text{tot}} = -0.41$, $\gamma_{\text{red}} = -1.55$, and $\gamma_{\text{frac}} = -1.12$; changes of +0.11, +0.05, and -0.06, respectively.

This suggests that our results are not grossly effected by our choice of method for estimating stellar masses,

and especially not by the use of color- as opposed to SED-derived stellar masses.

9.6. Other Potential Systematic Effects

Large Scale Structure and Field-to-Field Variance—One interesting test of the effect of field-to-field variance is to restrict our attention only to the MUSYC ECDFS coverage of the GOODS-CDFS region. For this 143 \square' sub-field, we find $\gamma_{\text{tot}} = -0.62$, $\gamma_{\text{red}} = -1.37$, and $\gamma_{\text{frac}} = -1.00$, differences of -0.10, +0.23, and +0.06 with respect to the full 816 \square' ECDFS. In comparison to the full ECDFS, the dearth of galaxies at $z_{\text{phot}} \sim 0.8$ is even more pronounced, and seems to extend over the range $0.8 < z_{\text{phot}} < 1.2$; this appears to be the main

driver of the strong change in γ_{red} . Conversely, if we exclude the significantly underdense GOODS area, we find $\gamma_{\text{tot}} = -0.49$, $\gamma_{\text{red}} = -1.60$, and $\gamma_{\text{frac}} = -1.10$; differences of $+0.03$, -0.00 , and -0.04 , respectively. Again, this analysis underscores the fact that measurements of the red fraction are more robust against the effects of large scale structure than those of the number densities themselves.

The $z \approx 0$ value—In §8.4, we have shown that the $z \approx 0$ comparison point is critical in providing most of the signal for $z \gg 0$ evolution in the massive galaxy population. We have also considered our results vary if we change the way we treat the $z \approx 0$ point. In our default analysis, we constrain the fits so that they pass through the $z \approx 0$ points, effectively using the $z \approx 0$ point to normalize the high-redshift measurements. Since the (Poisson statistical) errors on the $z \approx 0$ points are just a few percent, our results do not change significantly if we include the $z \approx 0$ points in the fits.

For our default analysis, we have approximately accounted for the effect of photometric redshift errors, as they apply to the $z \gg 0$ sample, on the $z \approx 0$ measurements; we have done this by randomly perturbing the masses and colors of $z \approx 0$ galaxies using the typical uncertainties for $z \gg 0$ galaxies, due to the use of photometric redshifts, and given in Figure 2. Systematic and random errors in the number densities both of all and of red galaxies are on the order of 5 %. If we do not account for the Eddington bias in this way, we find that $\gamma_{\text{tot}} = -0.46$ and $\gamma_{\text{frac}} = -1.16$, changes of 0.06 and -0.10 , respectively.

Correcting for Galactic Dust Extinction—Note that we have not included specific corrections for Galactic foreground dust extinction. The ECDFS was specifically chosen for its very low Galactic gas and dust column density; the suggested corrections for the optical bands are $\lesssim 0.05$ mag. These corrections are typically as large or larger than the uncertainties on the photometric zero-points themselves; it is for this reason that we have chosen not to apply these corrections. If we were to include these corrections, however, our derived values of γ_{tot} and γ_{frac} change by -0.03 and $+0.04$, respectively.

Including Spectroscopic Redshift Determinations—From among the thousands of spectroscopic redshift determinations that are publicly available in the ECDFS, we have robust z_{spec} s for just over 20 % (1669/7840) of galaxies in our main sample, and for 20 % (269/1297) of those with $0.2 < z_{\text{phot}} < 2.0$ and $M_* > 10^{11} M_\odot$. Repeating our analysis with this additional information included, our results do not change significantly: we find $\gamma_{\text{tot}} = -0.50$ and $\gamma_{\text{red}} = -1.70$, differences of just $+0.02$ and $+0.00$, respectively. Similarly, we show in Appendix B that our $z \lesssim 0.8$ results do not change by more than a few percent if we adopt photometric redshifts from COMBO-17 (Wolf et al. 2004; $\sigma_z = 0.035$).

Excluding X-ray-Selected Galaxies—Note that we have made no attempt to exclude Type I AGN or QSOs from our analysis. In order to discover how significant an omission this is, we have repeated our analysis excluding all those objects appearing in the X-ray selected catalogs of Szokoly et al. (2004) and Treister et al. (2008). This excludes 3.2 % (250/7840) of galaxies from our main sample, and 6.5 % (96/1482) from our $M_* > 10^{11} M_\odot$ sample. Given these numbers, it is perhaps unsurprising that

the exclusion of these objects does not greatly affect our results: γ_{tot} and γ_{frac} change by -0.07 and $+0.03$, respectively.

9.7. Quantifying Potential Systematic Errors — Summary

How, and how much, do our results depend on our analytical methods and experimental design? We have now described a rather large number of sensitivity tests, designed both to identify which aspects of our experimental design are crucial in determining our results, as well as to estimate the size of lingering systematic errors in our results. The results of many of these tests are summarized in Table 3. Clearly, these sorts of tests can provide a staggering array of ‘metadata’, offering insights to guide not only the interpretation of the present data and results, but also the design of future experiments.

As we have shown in §8.4, the systematic uncertainties in the γ s due to discrepancies between the treatment of $z \approx 0$ and $z \gg 0$ galaxies is on the order of ± 0.2 ; this is the single greatest potential source of systematic uncertainty. Since we have treated these two samples in a uniform manner, we do not consider this as a lingering source of systematic uncertainty.

The dominant sources of systematic uncertainty are, in order of importance: the method of deriving photometric redshifts ($\Delta\gamma_{\text{tot}} \approx 0.15$, $\Delta\gamma_{\text{frac}} \approx 0.15$); photometric calibration errors ($\Delta\gamma_{\text{tot}} \approx 0.05$; $\Delta\gamma_{\text{frac}} \approx 0.10$); incompleteness ($\Delta\gamma_{\text{tot}} \approx 0.1$, $\Delta\gamma_{\text{frac}} \approx 0$); the choice of photometric redshift template set ($\Delta\gamma_{\text{tot}} \approx 0.06$; $\Delta\gamma_{\text{frac}} \approx 0.06$); photometric methods ($\Delta\gamma_{\text{tot}} \approx 0.07$; $\Delta\gamma_{\text{frac}} \approx 0$); and stellar mass estimates ($\Delta\gamma_{\text{tot}} \approx 0.05$; $\Delta\gamma_{\text{frac}} \approx 0.05$). We can also, for example, dismiss incompleteness due to our K S:N criterion, contamination of the sample by QSOs, and minor details of our photometric redshift calculation as significant sources of systematic uncertainty.

In summary, we estimate the systematic errors on the measured values to be $\Delta\gamma_{\text{tot}} = 0.21$ and $\Delta\gamma_{\text{frac}} = 0.20$; these values have been obtained by adding the dominant sources of systematic error in quadrature. We note that previous studies have not generally taken (all) sources of systematic error into account in their analysis.

10. A FINAL INDEPENDENT CONSISTENCY CHECK: QUANTIFYING THE EVOLUTION OF BRIGHT, RED GALAXIES WITHOUT REDSHIFTS

Our goal in this paper has been to quantify the growth of massive galaxies in general, and of massive red galaxies in particular, over the past 10 Gyr, or since $z \sim 2$. We have now seen—not completely unexpectedly—that the use of photometric redshifts is potentially a major source of systematic error in such measurements. For this reason, in this section we present a complementary and completely independent measurement which does not rely on redshift information *at all*.

10.1. Selecting Red Galaxies in Redshift Intervals

Figure 13 shows evolutionary tracks for a passively evolving stellar population, in terms of observed colors in the MUSYC ECDFS bands. Specifically, we have used Pégase V2.0 (Le Borgne & Rocca-Volmerange 2002) models with a short star formation episode (e-folding timescale of 100 Myr), beginning with $Z = 0.004$

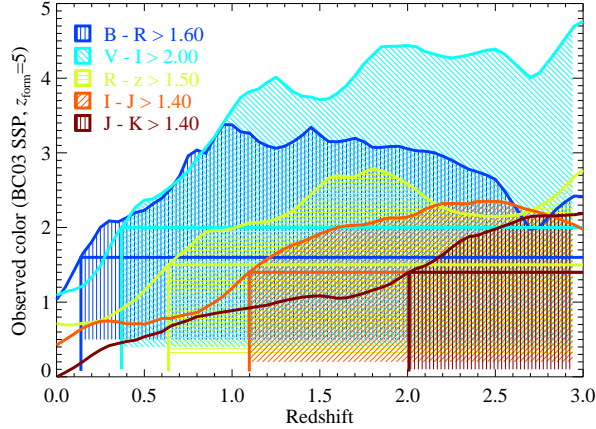


FIG. 13.— Evolutionary tracks, in terms of observed colors, for a passively evolving stellar population — Each track is for a synthetic Pégase V2.0 (Le Borgne & Rocca-Volmerange 2002) stellar population that evolves passively from $z_{\text{form}} = 5$; each of these tracks describe an approximate ‘red envelope’ for the true $z \lesssim 2$ color–redshift distribution. The sharp rise in each track is due to the Balmer and/or 4000 Å breaks becoming redshifted between the two observed filters. The shaded regions show where each of the four observed color criteria given will select red galaxies; taken together, they therefore provide a means for selecting passive galaxies in rough redshift bins (see also §10.2).

at $z_{\text{form}} = 5$, and ending with $Z \approx Z_{\odot}$. This (approximately) maximally old model describes a ‘red envelope’ for the colour–redshift relation for observed galaxies: at a given redshift only extreme dust extinction can produce observed colors redder than these tracks.

As is evident in this figure, as the Balmer and/or 4000 Å breaks are first redshifted between the observed bands, there is a sharp rise in the observed colour — by selecting objects that are very red in a certain colour, it is thus possible to select galaxies that lie beyond a certain redshift. This is completely analogous to the ERO (McCarthy 2004, and references therein) or DRG (Franx et al. 2003) selection criteria for red galaxies at moderate-to-high redshifts. The particular selections we have adopted in Figure 13 (and given in Col. 1 of Table 4) translate to minimum redshifts of approximately 0.16, 0.40, 0.66, 1.12, and 2.05.

By applying several of these colour criteria in concert, with the reddest criteria given primacy, it is then possible to select red galaxies in rough redshift intervals: the highest redshift galaxies are selected by the criterion $(J-K) > 1.4$; then, the next highest redshift galaxies are then selected from the remaining set (*ie.* $(J-K) < 1.4$) by the criterion $(I-J) > 1.4$, and so on. In the current context, this can be thought of as a two-colour, binned photometric redshift.

The prevalence of objects selected in this way are given in Col. 4 of Table 4. To our limit of $K < 22$, we find 386, 655, 690, 304, and 286 objects selected by this tiered set of colour criteria.

10.2. Interpreting the Numbers of Colour Selected Galaxies

It is clear that the exact redshift range over which a galaxy might satisfy a given color criterion depends on that galaxy’s SED: as well as passively evolving galax-

TABLE 4
QUANTIFYING THE EVOLUTION OF BRIGHT, RED GALAXIES WITHOUT REDSHIFTS

Color Criterion (1)	Redshift		Prevalence		
	z_{low} (2)	$\langle z \rangle$ (3)	Observed (4)	Expected (5)	Relative (6)
$B - R > 1.6$	0.1	0.3	0.47 / □	0.76 / □	62 %
$V - I > 2.0$	0.4	0.6	0.80 / □	1.80 / □	45 %
$R - z > 1.5$	0.6	0.9	0.84 / □	1.94 / □	43 %
$I - J > 1.4$	1.1	1.4	0.37 / □	1.29 / □	29 %
$J - K > 1.4$	2.0	2.6	0.35 / □	1.55 / □	23 %

NOTE. — We have used a tiered set of color selection criteria (Col. 1) to select red galaxies in approximate redshift intervals. Here, it is understood that redder criteria are given primacy; for example, objects counted in the second row may or may not satisfy the first criterion, but do not satisfy any of the three subsequent criteria. We give the minimum and mean redshifts of color-selected galaxies from the synthetic, ‘passive evolution’ catalog in Col.s (2) and (3), respectively. The observed prevalence of color-selected objects in the MUSYC ECDFS catalog are given in Col. (4); Col. (5) gives the same quantity for the synthetic catalog. The ratio of the two is given in Col. (6), which gives an estimate of the relative number of (potentially) passively evolving galaxies at different redshifts.

ies, these selections will also include galaxies whose red observed colors are due to, *e.g.*, dust obscuration or considerably higher redshifts. Thus, the details of the evolving, bivariate color–magnitude distribution is folded into the numbers of color-selected galaxies. For this reason, we are forced to interpret the numbers of color-selected galaxies with reference to a particular model for the evolution of red galaxies.

This is done as follows: we construct a mock catalog in which galaxies’ luminosities are distributed according to the $z \approx 0$ luminosity function for red galaxies, which we have determined from the low- z sample, as analyzed in Appendix A. This luminosity function is nearly identical to that of Blanton et al. (2005c); our results do not change significantly adopting the red galaxy luminosity functions from either Bell et al. (2003) or Cole et al. (2001). Galaxies are placed randomly (*ie.* uniform comoving density) in the volume $z < 5$. Next, we generate synthetic photometry for each object in the catalog using the set of Pégase V2.0 (Le Borgne & Rocca-Volmerange 2002) models shown in Figure 13, which are essentially passively evolving from $z_{\text{form}} = 5$. We also include typical errors for the MUSYC ECDFS catalog, to approximately account for photometric scatter. Finally, we apply our colour selection criteria to this catalog, exactly as for the observed ECDFS catalog. The predicted prevalence of colour selected galaxies, to be compared to those observed, are given in the Col. 5 of Table 4.

Whereas all red galaxies are assumed to evolve passively in the synthetic reference catalog, the real color selected samples will include dusty or high-redshift star-forming galaxies: while all passive galaxies are red, not all red galaxies are passive. As we argue in §8.1, the number of color selected galaxies can therefore be used to place an upper limit on the number of passively evolving galaxies, since these color criteria should select a

complete but contaminated sample of genuinely passive galaxies.

The results presented in Table 4 thus suggest that the number density of bright, passively evolving galaxies has increased by a factor of at least ~ 2 since $z \sim 1$. Moreover, we find that the number density of passive galaxies in the range $1 \lesssim z \lesssim 2$ is at most $\sim 25\%$ of the present day value. Taken at face value, this would suggest that at most $1/4$ present day red sequence galaxies can have evolved passively from $z \sim 2$; the remainder were still forming, whether through star formation or by the hierarchical assembly of undetected, and thus fainter, subunits, or some combination of the two.

Finally, we emphasize the essential simplicity of this analysis, and thus its suitability for comparisons between different datasets, which may use different strategies for the computation of photometric redshifts, restframe colors, stellar masses, and so on.

10.3. Tying it all Together

Our final task is to compare the results of this section with those in §8; we do this in Figure 14. In this plot, the abscissa is the effective wavelength of the bluer of the two filters used in each color criterion; the ordinate is the number of color selected galaxies observed in the MUSYC ECDFS catalog, relative to the expectation for passive evolution. The yellow squares refer to the $z_{\text{form}} = 5$ model shown in Figure 13 and presented in Table 4. The blue triangles and red pentagons show how these results would vary had we assumed $z_{\text{form}} = 4$ and $z_{\text{form}} = 6$, respectively.

The specific redshift range that is selected by each color criterion depends on the particular tracks used. For a given color criterion, the mean redshift of selected sources (derived from the synthetic ‘passive evolution’ catalog) thus varies for different choices of z_{form} : approximate transformations are given for each scenario at the top of the Figure.

Finally, the solid line shows our fit results for the $z_{\text{phot}} \lesssim 2$ number density evolution of red galaxies, shown in Figure 10. In order to put this curve on this plot, we have used the mean redshift of (synthetic, passive) color-selected sources assuming passive evolution from $z_{\text{form}} = 5$. Given the very different assumptions and methods lying behind these two results, the agreement is very impressive.

Both analyses clearly indicate that the number of red galaxies at $z \approx 0.7$ is approximately 50 % of the present day value; at $z \approx 1.5$, it is approximately 25 %. In other words, at most, approximately $1/2$ local red sequence galaxies were already ‘in place’ by $z \approx 0.7$, and have evolved passively since that time; at $z \approx 1.5$, at most $1/4$ were in place.

11. SUMMARY AND CONCLUSIONS

We have presented the color–magnitude (Figure 4) and color–stellar mass diagrams (Figure 5) for $z \lesssim 2$, based on a sample of $K < 22$ galaxies drawn from the MUSYC catalog of the ECDFS. On the basis of the ten band SEDs, we achieve a photometric redshift accuracy of $\sigma_z = 0.036$ (Figure 1); this figure represents the current state of the art for broadband photometric look-back surveys. We have used an empirical argument to

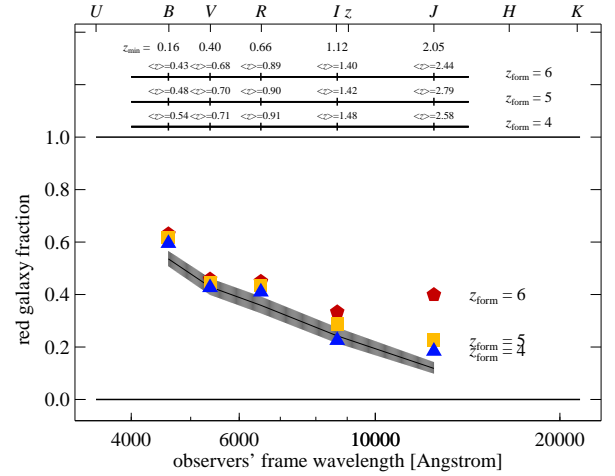


FIG. 14.— Quantifying the number evolution of bright, red galaxies without redshifts—The observed numbers of color-selected galaxies, relative to the number expected for passive evolution, plotted as a function of the effective wavelength of the bluer filter used in the selection criterion; the criteria themselves are given in Table 4. The ordinate in this plot is essentially the number of galaxies with colors that are consistent with passive evolution from z_{form} , relative to the number of $z \approx 0$ red sequence galaxies; we have plotted results assuming $z_{\text{form}} = 4$ (blue triangles), 5 (yellow squares), and 6 (red pentagons). The mean redshift of color selected galaxies, as derived from the synthetic ‘passive evolution’ catalog, does depend mildly on the choice of evolutionary scenario. The mean redshift of galaxies selected by each criterion, $\langle z \rangle$, is given separately for each choice of z_{form} at the top of the Figure. The minimum redshift is more robust; this is given as z_{min} . Lastly, the solid line and shaded region show the fit to the $z_{\text{phot}} \lesssim 2$ evolution in the number density of massive red galaxies, derived in §8 (see Figure 10); the shaded region shows the 1σ uncertainty in the fit. (To put this relation on this plot, we have used the $z_{\text{form}} = 5$ catalog to map each color criterion to $\langle z \rangle$.) The agreement between these two very different calculations is impressive.

demonstrate that our main galaxy sample is approximately complete (volume limited) for $M_* > 10^{11}$ and $z_{\text{phot}} < 1.8$ (Figure 3).

Based on the joint color–stellar mass–redshift distribution of this mass-selected sample, we make the following conclusions:

1. The color distribution of the massive galaxy population is well described by the sum of two separate Gaussian distributions for $z_{\text{phot}} \lesssim 1.2$ (Figure 6). Beyond this redshift, the depth of our NIR data makes it impossible to identify distinct red and blue subgroups from within the general massive galaxy population on the basis of the observed color distribution. The question as to the existence or otherwise of a $z_{\text{phot}} \gtrsim 1.5$ red sequence will require data approximately an order of magnitude deeper than our own (Figure 7).
2. The colors of red sequence galaxies have become progressively redder by ~ 0.5 mag since $z_{\text{phot}} \approx 1.1$ (Figure 8). Making a linear fit to the observed evolution, we find $\Delta(u - r) \propto (-0.44 \pm 0.02) z_{\text{phot}}$. Simple models can only describe the observations assuming sub-solar metallicities (Figure 9): it remains a challenge to consistently describe the observed colors and the mass–metallicity relation.

3. While the number density of massive galaxies evolves mildly for $z_{\text{phot}} \lesssim 2$, we see strong evolution in the red galaxy fraction. That is, the massive galaxy population appears to be *changing* more than it is *growing*. We have quantified this evolution using parametric fits of the form $(1+z)^\gamma$. For $z_{\text{phot}} < 1.8$, we find $\gamma_{\text{tot}} = -0.52 \pm 0.12(\pm 0.20)$, $\gamma_{\text{red}} = -1.60 \pm 0.14(\pm 0.21)$, and $\gamma_{\text{frac}} = -1.06 \pm 0.16(\pm 0.21)$.

The systematic errors (given in brackets above) have been derived on the basis of a whole raft of sensitivity analyses, and are due primarily to photometric calibration errors and systematic effects arising from the photometric redshift calculation (§9).

Finally, in §10, we showed that these results are completely consistent with an independent analysis based only on directly observed quantities; that is, without deriving redshifts, etc., for individual galaxies.

The two major advances in this work are the quantification of the $z_{\text{phot}} \lesssim 1.2$ color evolution of the red galaxy sequence as a whole, and the quantification of the $z_{\text{phot}} \lesssim 2$ evolution of the red fraction among $M_* > 10^{11} M_\odot$ galaxies.

Knowing that the vast majority of $10^{11} M_\odot$ galaxies in the local universe fall on the red sequence (Figure 6), we can identify our massive galaxy sample as the immediate progenitors of local red sequence galaxies. Further, by extrapolating the observed $z_{\text{phot}} < 1.4$ color evolution

of the red sequence to higher redshifts, we can identify our ‘red’ galaxies as those which *potentially* have already found their place on the red sequence: the high redshift analogues of local red sequence galaxies. However, simply selecting ‘red’ galaxies may include a significant number of galaxies whose red colors are due to heavy dust obscuration, we argue that our red galaxy measurements provide an approximate upper limit on the number of passive or quiescent galaxies.

With this assumption, our results suggest that at least 1/2 of all $M_* \gtrsim 10^{11} M_\odot$ galaxies joined (or rejoined) the red sequence only after $z \sim 1$, and that at most 1/5 massive galaxies have resided on the red sequence since $z \sim 2$. These results provide new constraints for quenching models, such as quasar and “radio mode” AGN feedback (Croton et al. 2006; Cattaneo et al 2006). Establishing which of our ‘red’ galaxies are genuinely ‘red and dead’ offers the opportunity to considerably tighten these constraints.

This work was supported through grants by the Nederlandse Organisatie voor Wetenschappelijk Onderzoek (NWO), the Leids Kerkhoven-Bosscha Fonds (LKBF), and National Science Foundation (NSF) CAREER grant AST 04-49678. We also wish to thank the organizers and participants of the several workshops hosted by the Lorentz Center, where many aspects of this work were developed and refined. SW gratefully acknowledges support from the W M Keck Foundation.

REFERENCES

- Arnouts S et al., 2001, A&A 379, 740
 Arnouts S et al., 2007, A&A 476, 137
 Baldry I K, Glazebrook K, Brinkmann J, Ivezić Ž, Lupton R H, Nicol R C, Szalay A S, 2004, ApJ 600, 694
 Baldry I K, Balogh M L, Bower R G, Glazebrook K, Nichol R C, Bamford S P, Budavari T, 2006, MNRAS 373, 469
 Balogh M L, Baldry I K, Nichol R, Miller C, Bower R, Glazebrook K, 2003, ApJ 615, L101
 Bell E F, de Jong R S, 2001, ApJ 550, 212
 Bell E F, McIntosh D H, Katz N, Weinberg M D, 2003, ApJS 149, 289
 Bell E F et al., 2004, ApJ 600, L11
 Bell E F et al., 2004, ApJ 608, 752
 Bell E F, Zheng X Z, Papovich C, Borch A, Wolf C, Meisenheimer K, 2007, ApJ (in press)
 Benítez N, 2000, ApJ 536, 571
 Bertin E & Arnouts S, A&A 117, 393
 Blanc G A et al., 2008, ApJ, submitted
 Blanton M R et al., 2003, ApJ 594, 186
 Blanton M R, Eisenstein D, Hogg D W, Schlegel B K, Brinkmann J, 2005, ApJ 629, 143
 Blanton M R, Schlegel D J, Strauss M A, Brinkmann J, Finkbeiner D, Fukugita M, Gunn J E, Hogg D W, Ivezić Ž, Knapp G R, Lupton R H, Munn J A, Schneider D P, Tegmark M, Zehavi I, 2005, AJ 129, 2562
 Blanton M R, Lupton R H, Schlegel D J, Strauss M A, Brinkmann, Fukugita M, Loveday J, 2005, ApJ 631, 208
 Blanton M R & Roweis S, 2007, ApJ 133, 734
 Bolzonella M, Miralles J-M & Pelló R, 2000, A&A 363, 476
 Borch A, Meisenheimer K, Bell E F, Rix H-W, Wolf C, Dye S, Kleinheinrich M, Kovacs Z, Wisotzki L, 2006, A&A 453, 869
 Brammer G B, Van Dokkum P G, Coppi P, 2008, submitted
 Brinchmann J, Charlot S, White S D M, Tremonti C, Kauffmann G, Heckman T, 2004, MNRAS 351, 1151
 Brown M J I, Dey A, Jannuzi B T, Brand K, Benson A J, Brodwin M, Croton D J, Eisenhardt P R, 2007, ApJ 164, 858
 Brown M J I, Zheng Z, White M, Dey A, Jannuzi B T, Benson A J, Brand K, Brodwin M, Croton D J
 Bruzual G, Charlot S, 2003, MNRAS 344, 1000
 Bruzual G A, 2008, astro-ph/0703052 (v2)
 Bundy K et al., 2006, ApJ 651, 120
 Cattaneo A, Dekel A, Devriendt J, Guiderdoni B, Blaizot J, 2006, 370, 1651
 Cattaneo A, Dekel A, Faber S M, Guiderdoni B, 2008, MNRAS (submitted), arXiv:0801.1673
 Cimatti A, Mignoli M, Daddi E, Pozzetti L, Fontana A, Saracco P, Poli F, Renzini A, Zamorani G, Broadhurst T, Cristiani S, D’Odorico S, Giallongo E, Gilmozzi R, Menci N, 2002, A&A 392, 395
 Cirasuolo M, McLure R J, Dunlop J S, Almaini O, Foucaud S, Smail I, Sekiguchi K, Simpson C, Eales S, Dye S, Watson M G, Page M J, Hist P, 2007, MNRAS 380, 585
 Cole S et al., 2001, MNRAS 326, 255
 Coleman G D, Wu C C, Weedman D W, 1980, ApJS 43, 393
 Connolly A J, Szalay A S, Dickinson M, Subbarao M U, Brunner R J, 1997, ApJ 486, L11
 Conselice C J, Bundy K, Trujillo I, Coil A, Eisenhardt P, Ellis R S, Georgakakis A, Huang J, Lotz J, Nandra K, Newman J, Papovich C, Weiner B, Willmer C, 2007, MNRAS 381, 962
 Cooper M J et al., 2007, MNRAS 376, 1445
 Croton D J, Springel V, White S D M, De Lucia G, Frenk C S, Gao L, Jenkins A, Kauffmann G, Navarro J F, Yoshida N, 2006, MNRAS 365, 11
 Daddi E et al., 2005, ApJ 626, 680
 Damen M et al., 2008, ApJ (submitted)
 Dekel A, Birnboim Y, 2006, MNRAS 368, 2
 De Lucia G et al., 2007, MNRAS 374, 809
 Dickinson M E, Giavalisco M, et al., 2002, astro-ph/0204213 (v1)
 Driver S P, Allen P D, Graham A W, Cameron E, Liske J, Ellis S C, Cross N J G, De Propris R, Phillipps S, Couch W J, 2006, MNRAS 368, 414
 Drory N et al., 2004, ApJ 608, 742
 Ellis S C, Driver S P, Allen S D, Liske J, Bland-Hawthorn J, De Propris R, 2005, MNRAS 363, 1257
 Erben T et al., 2005, AN 326, 432
 Faber S M et al., 2007, ApJ 665, 265
 Fontana A et al., 2004, A&A 424, 23
 Fontana A et al., 2006, A&A 459, 745
 Förster-Schreiber N M, Franx M, Labbé I, Rudnick G, Van Dokkum P G, Illingworth G D, Kuijken K, Moorwood A F M, Rix, H.W., Röttgering H, Van der Werf P, 2006, AJ 131, 1891
 Franx M et al., 2003, ApJ 587, L79
 Franzetti P et al., 2007, A&A, 165, 711
 Gawiser E et al., 2006, ApJS 162, 1
 Giacconi R, Rosati P, Tozzi P, Nonino M, Hasinger G, Norman C, Bergeron J, Borgani S, Gilli R, Gilmozzi R, Zheng W, 2001, ApJ 551, 624

- Grazian A, Fontana A, De Santis C, Nonino M, Salimbeni S, Giallongo E, Cristiani S, Gallozzi S, Vanzella E, 2006, *A&A* 449, 951
- Gronwall C et al., 2007, *ApJ*, 667, 79
- Gunn J E & Stryker L L, 1983, *ApJSS* 52, 121
- Hildebrandt H et al., 2006, *A&A* 452, 1121
- Hogg D W, Blanton M R, Eisenstein D J, Gunn J E, Schlegel D J, Zehavi I, Bahcall N A, Brinkmann J, Csabai I, Schneider D P, Weinberg D H, York D G, 2003, *ApJ* 585, L5
- Hopkins A M, 2004, *ApJ* 615, 209
- Im M et al., 2002, *ApJ* 571, 136
- Juneau S et al., 2005, *ApJ* 619, L135
- Kauffman G, Heckman T M, White S D M, Charlot S, Tremonti C, Peng E W, Seibert M, Brinkmann J, Nichol R C, Subba Rao M, York D, 2003, *MNRAS* 341, 54
- Kinney A L, Calzetti D, Bohlin R C, McQuade K, Storch-Bergmann T, Schmitt H R, 1996, *ApJ* 467, 38
- Koposov et al., 2008 (in prep.)
- Kriek M, et al., 2006, *ApJ*, 649, L71
- Kriek M, Van der Wel A, Van Dokkum P G, Franx M, Illingworth G D, 2008, *ApJ* (accepted); arXiv:0804.4175v1
- Kroupa P, 2001, *MNRAS* 322, 231
- Labbé I et al., 2003, *AJ* 125, 1107
- Labbé I et al., 2005, *ApJ* 624, L81
- Labbé I, Franx M, Rudnick G, Forster Schrieber N M, Van Dokkum P G, Moorwood A, Rix H-W, Rottgering H, Trujillo I, Van der Werf P, 2007, *ApJ* 665, 964
- Lawrence A et al., 2007, *MNRAS* 379, 1599
- Le Borgne D & Rocca-Volmerange B, 2002, *A&A* 386, 466
- Le Fèvre O et al., 2004, *A&A* 428, 1043
- Lilly S, Le Fèvre O, Hammer F, Crampton D, 1996, *ApJ* 460, L1
- Lin L et al., 2007, *ApJ* 660, L51
- Madau P, Ferguson H C, Dickinson M E, Giallisco M, Steidel C C, Fruchter A, 1996, *MNRAS* 283, 1388
- Maraston C, 2005, *MNRAS* 362, 799
- McCarthy P J, 2004, *ARAA*, 42, 477
- McGrath E J, Stockton A, Canalizo G, 2007, *ApJ* 669, 241
- Menci N, Fontana A, Giallongo E, Salimbeni S, 2005, *ApJ* 632, 49
- Moy E et al., 2003, *A&A* 403, 493
- Nagamine K, Ostriker J P, Fukugita M, Cen R, 2006, *ApJ* 653, 881
- Panther B, Jimenez R, Heavens A F, Charlot S, 2007, *MNRAS* 378, 1550
- Pérez-González P G et al., 2008, *ApJ* 675, 234
- Popesso P et al., 2008, arXiv:0802.2930v1
- Pozzetti L et al., 2007, *A&A*, 474, 447
- Quadri R et al., 2007, *AJ* 134, 3
- Ravikumar C D et al., 2006, *A&A* 465, 1099
- Reddy N A, Steidel C C, Fadda D, Yan L, Pettini M, Shapley A E, Erb D K, Adelberger K L, 2006, *ApJ* 644, 792
- Rix H-W et al., 2004, *ApJSS* 152, 163
- Rudnick G et al., 2003, *ApJ* 599, 847
- Ruhland C, Bell E F, Häußler B, Taylor E N, Barden M, McIntosh D, 2008, submitted
- Salpeter E E, 1955, *ApJ* 121, 161
- Scarlata C et al., 2008, *ApJSS*, 172, 510
- Somerville R S, Lee K, Ferguson H, Gardner J P, Moustakas L A, Giallisco M, 2004, *ApJ* 600, L171
- Strateva I et al., 2001, *AJ*, 122, 1861
- Szokoly G P et al., 2004, *ApJSS* 155, 271
- Taylor E N et al., 2008 (Paper I), *ApJSS* (submitted)
- Teister E, Virani S, Gawiser E, Urry C M, Lira P, Francke H, Blanc G A, Cardamone C N, Damen M, Taylor E N, Schawinski K
- Tremonti C A et al., 2004, *ApJ* 613, 898
- Tresse L et al., *A&A* 472, 403
- Van der Wel A, Franx M, Van Dokkum P G, Rix H-W, Illingworth G D, Rosatti P, 2005, *ApJ* 631, 145
- Van der Wel A, 2008, *ApJ* 675, L13
- Van Dokkum P G & Franx M, 2001, *ApJ* 553, 90
- Van Dokkum P G et al., 2006, *ApJ* 638, 59
- Vanzella et al., 2008, *A&A* 471, 83
- Weiner B J et al., 2005, *ApJ* 620, 595
- Willmer C N A et al., 2006, *ApJ*, 647, 853
- Wolf C et al., 2004, *A&A* 421, 913
- Wolf C, Hildebrandt H, Taylor E N, Meisenheimer K, 2008, *A&A* (submitted), arXiv:0809.2066
- Wuyts S et al., 2008, *ApJ* (in press), arXiv:0804.0615v2
- Wyder T K, 2007, *ApJSS* 173, 293
- York D G et al., 2000, *ApJ* 120, 1579

APPENDIX

A. THE $Z = 0$ COMPARISON POINT

In this Appendix, we describe the process by which we have derived the $z \approx 0$ number density of massive galaxies in general, and of red galaxies in particular, from the low- z subsample of the New York University (NYU) Value Added Galaxy Catalog (VAGC) from the Sloan Digital Sky Survey (SDSS) data release 4 (DR4); this catalog has been compiled and described by Blanton et al. (2005b). We will refer to this sample simply as the ‘low- z ’ sample, as opposed to the ‘high- z ’, K-selected sample in the main text. The overarching concern is uniformity in the analysis of the low- z and high- z samples, where possible and appropriate, in order to make as fair as possible a comparison between the high- z and low- z data. Our discussion proceeds in three parts: first, we describe our analysis of low- z galaxies; we then describe our characterisation of the galaxy red sequence; finally, we give our derived number density of massive galaxies at $z \approx 0$, including mimicking the effects of the random photometric redshift errors typical for the $z \gg 0$ sample.

A.1. Low- z Galaxy Analysis

For each galaxy in the low- z sample, we have constructed a *ugriz* SED using ‘model’ magnitudes (measured by fitting either an exponential or $r^{1/4}$ profile in each band, with structural parameters derived from the *i* band image) as given in the low- z catalog. In analogue to high- z galaxies, these SEDs are then scaled up to the ‘Petrosian’ r magnitude. The Petrosian apertures are designed to measure a fixed fraction of a galaxy’s light, irrespective of brightness or distance, but with some dependence on the light distribution: neglecting the effects of seeing, the Petrosian aperture captures 99 % of the total light for an exponential profile, compared to $\gtrsim 80$ % for a de Vaucouleurs profile (Blanton et al. 2005b). We make no attempt to correct for missed flux, but note that similar effects are present at a similar level in our own data (see §9.2.2). Following (Blanton et al. 2005b), we use the following factors to correct the basic SDSS calibration to AB magnitudes: (-0.042, +0.036, +0.015, +0.013, -0.002) for (u , g , r , i , z).

We have derived restframe photometry and stellar masses for low- z galaxies using exactly the same machinery as for the high- z sample, adopting the heliocentric redshifts given in the low- z catalog. Our interpolated restframe *ugriz* photometry agrees quite well with that given by Blanton et al. (2005b) in the low- z catalog. (Whereas we use galaxy color-color relations, based on six empirical galaxy template spectra, to interpolate restframe photometry, Blanton et al. (2005b) determine restframe fluxes by fitting a non-negative linear combination of five carefully chosen synthetic spectra, and then integrating the best fit spectrum.) On average, in comparison to Blanton et al. (2005b), our $u - r$ colors are ~ 0.02 mag bluer for blue galaxies and ~ 0.03 mag redder for red galaxies. We calculate the distance modulus using the proper motion corrected redshifts given in the catalog. Finally, we have derived stellar masses based on the interpolated restframe B and V fluxes, using Equation 1.

A.2. The Red Galaxy Sequence at $z = 0$

Figure A1 shows our CMD (*left*) and CM_{*}D (*right*) diagrams for the general $z \approx 0$ field galaxy population; in each panel, the logarithmic greyscales show the data density. We note that these two plots are very nearly equivalent: the CM_{*}D can be seen as simply a ‘sheared’ version of the CMD, with the bluer galaxies dragged further towards the left. A separate red galaxy sequence is easily discernible in each panel.

We have characterized this red galaxy sequence, as a function of magnitude or of mass, by taking a narrow slices in either absolute magnitude or stellar mass, and fitting double Gaussians to the color distribution in each bin. The results of these fits are shown in each panel of Figure A1 as the red and blue contours. This gives some indication of the relative numbers of red and blue galaxies as a function of magnitude/mass. In order to characterize the separate red and blue populations, we also show the center and width of each Gaussian fit as the yellow and cyan points and error bars.

In order to determine the slope of the high luminosity/mass end of the red sequence CMR and CM_{*}R, we have simply made linear fits to the centers of the $M_r < -21$ and $M_* > 10^{10.5} M_\odot$ ‘red’ distributions. The results of these fits are:

$$(u - r) = 2.612 - 0.090 \times (M_r + 22) = 2.573 + 0.237 \times \log_{10}(M_*/10^{11} M_\odot). \quad (\text{A1})$$

These relations are shown as the solid black lines in each panel. Finally, in order to make some distinction between ‘red’ and ‘blue’ galaxies which could be easily applied to the high- z sample, we simply use a cut 0.25 mag bluer than this relation. In each panel, this cut can be seen to approximately coincide with the so-called ‘green valley’ between the red and blue galaxy populations.

Finally, in the inset of each diagram, we show the color distribution for the brightest ($M_r < -21$) or most massive ($M_* > 10^{11} M_\odot$) galaxies, after subtracting away the color-magnitude or color-stellar mass relations given by Equation A1. (See also 6.) We also show double Gaussian fits to these distributions, which are the basis for the $z \approx 0$ points shown in Figures 8 and 9. We note in passing that, at least for $-19 \gtrsim M_r \gtrsim -21.5$, the width of the color distributions of red and blue galaxies is not a strong function of magnitude: $\Delta(u - r) \sim 0.12$, and $\Delta(u - r) \approx 0.20$ for red and blue galaxies, respectively.

A.3. The Number Density of Massive Galaxies at $z \approx 0$

For our purposes (see §8), the crucial final quantity is the number density of massive galaxies at $z \approx 0$. We find that the number density of $M_* > 10^{11} M_\odot$ galaxies is $(6.64 \pm 0.38) \times 10^{-4} h^3 \text{ Mpc}^{-3}$; for (u, r) red galaxies, the number is $(6.07 \pm 0.36) \times 10^{-4} h^3 \text{ Mpc}^{-3}$. This measurement is not significantly affected by either volume or surface brightness incompleteness. Compared to the more sophisticated analyses of Bell et al. (2003) and Cole et al. (2001), our value for the number density of massive galaxies is 10 % higher and 25 % lower, respectively.

As we have repeatedly stressed, our prime concern is uniformity in the analysis of the low- and high- z samples. Photometric redshift errors are a major source of uncertainty for the high- z sample — how would comparable errors affect the low- z measurements? Given the redshift range of our low- z galaxies ($0.003 < z < 0.05$) and the estimated photometric redshift errors among high- z galaxies ($\Delta z/(1+z) \sim 0.035$), it would be inappropriate to simply apply typical redshift errors and repeat our calculations: this would effectively throw away all distance information. Instead,

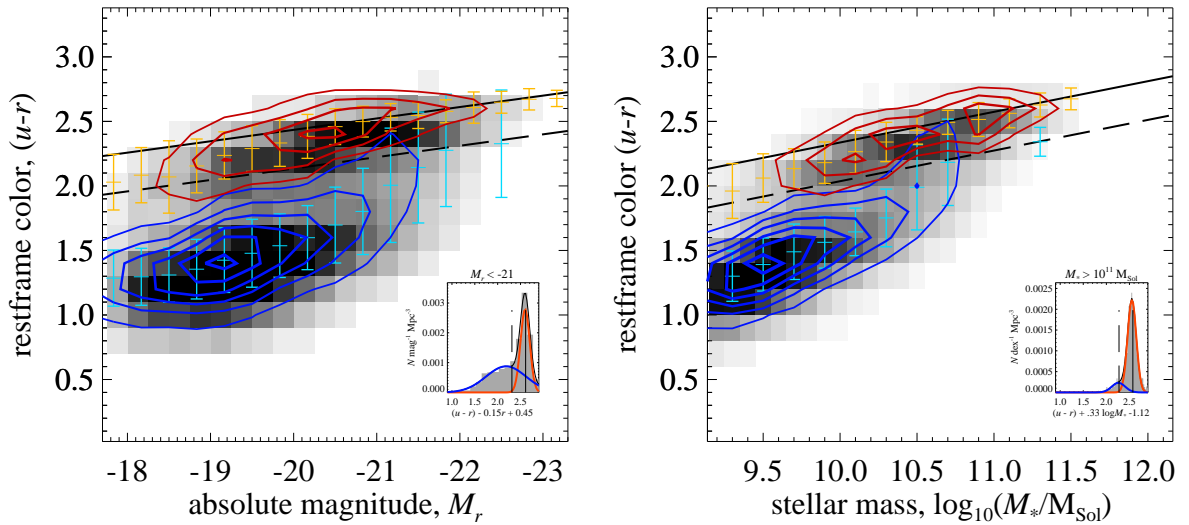


FIG. A1.— The ‘low z ’ sample from the NYU VAGC of the SDSS (DR4), used to derive the $z \approx 0$ comparison point for the main, ‘high z ’ sample discussed in the text—Color-magnitude (*left*) and color-stellar mass (*right*) diagrams — The greyscale shows the density of points. The errors bars show the center and width of the color distributions of the red and blue populations, obtained from double Gaussian fits in narrow magnitude/mass slices. These fits to the populations are also represented by the logarithmic (0.5 dex) contours, to give some idea of the data density of red/blue galaxies.

what we have done is to apply the typical uncertainties on M_r , $(u-r)$ and M_* due to photometric redshift errors, as shown in Figure 2. For simplicity, we have ignored correlations between these errors.

In line with our earlier findings, including the effects of photometric redshift errors makes less of a difference to measurements based on stellar masses than to those based on absolute magnitudes. Our fits to the red sequence become:

$$(u-r) = 2.608 - 0.113 \times (M_r + 22) = 2.577 + 0.223 \times \log_{10}(M_*/10^{11} \text{ M}_\odot). \quad (\text{A2})$$

Our measurements of the $z \approx 0$ number density of galaxies more massive than 10^{11} M_\odot becomes $(6.93 \pm 0.38) \times 10^{-4} h^3 \text{ Mpc}^{-3}$ in total, and $(5.86 \pm 0.35) \times 10^{-4} h^3 \text{ Mpc}^{-3}$ for red sequence galaxies. That is, the effects of the redshift errors expected among $z \gg 0$ galaxies affect the measurement of the $z \approx 0$ number density by less than 5 %.

These numbers, approximately accounting for the Eddington bias due to photometric redshift errors (as they apply to the $z \gg 0$ sample), are then what have used as a local reference value to compare to the $z \gg 0$ data.

B. A DETAILED COMPARISON WITH COMBO-17

In the ECDFS, the COMBO-17 and MUSYC datasets represent parallel analytical paths describing the same physical reality—indeed the COMBO-17 broadband observations form the foundation of the MUSYC raw optical data. Ideally, then, the two surveys’ results should agree identically; instead, in comparison to COMBO-17, the MUSYC results suggest 40 % more massive ($M_* > 10^{11} \text{ M}_\odot$) galaxies at $0.2 < z_{\text{phot}} < 0.8$ —a degree of difference more on a par with that expected from field-to-field variation. In this Appendix, we identify the main cause of this discrepancy.

B.1. Photometric Redshift Accuracy: MUSYC photometry with COMBO-17 redshifts

The essential differences between the COMBO-17 and MUSYC datasets are COMBO-17’s twelve medium bands, allowing much more precise photometric redshift determinations for $z \lesssim 1$, and the MUSYC $z'JHK$ data, which open the door to the $z \gtrsim 1$ universe. The first and most obvious concern is thus that the difference between the two surveys’ $z_{\text{phot}} \lesssim 1$ results are a product of their different photometric redshift accuracies. To test this, we have tried simply adopting the COMBO-17 photometric redshifts in place of our own determinations, and repeated our analysis.

The results of this test are shown in Figure B1: the main panel shows our primary result (*viz.*, the number density of $M_* > 10^{11} \text{ M}_\odot$ galaxies as a function of redshift; see Figure 10). The solid histograms show this trial re-analysis of the MUSYC data adopting COMBO-17 redshifts; this should be compared to the fiducial results from MUSYC (*dashed histogram*) and COMBO-17 (*dotted histograms*). We have derived these ‘COMBO-17’ results from the public catalog presented by Wolf et al. (2003), supplemented with the stellar mass determinations used by Borch et al. (2006).

At least for $z_{\text{phot}} < 0.8$, the use of COMBO-17 redshifts in place of our own does not have a great effect on our results: the solid histograms lie quite close to the dashed ones. Quantitatively, adopting COMBO-17 redshifts in place of our own leaves the number of $M_* > 10^{11} \text{ M}_\odot$ galaxies over $0.2 < z_{\text{phot}} < 0.8$ unchanged to within 1 %; the effect is slightly greater for the red population, leading to a red fraction that is 17 % higher over the same interval. This

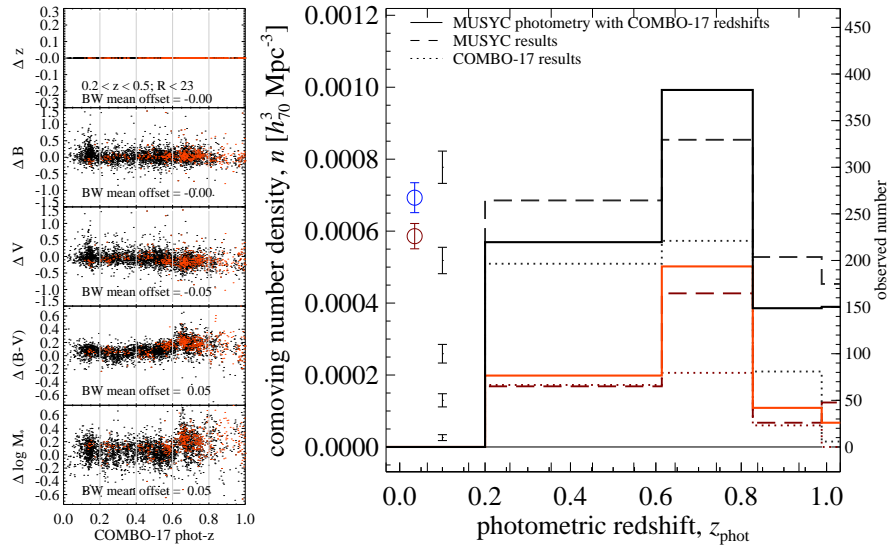


FIG. B1.— Reanalysis of the MUSYC data adopting redshifts from COMBO-17—*Main panel*: The measured number density of $M_* > 10^{11} \text{ M}_\odot$ galaxies for $z \lesssim 1$ based on the MUSYC photometry, but adopting redshifts from the COMBO-17 catalog in place of our own (*solid histograms*). These results should be compared to the fiducial results from MUSYC (*dashed histograms*) and from COMBO-17 (*dotted histograms*). The red and black histograms are for red and all galaxies, respectively. Where the COMBO-17 and MUSYC results differ by 40 %, the effect of using of COMBO-17 redshifts is less than 10 %; the difference between the two surveys’ results cannot be explained by differences in the photometric redshifts. *Left panels*: the difference between the (from top to bottom) photometric redshifts, absolute B and V magnitudes, restframe $(B-V)$ colors, and stellar masses used to produce the results shown in the main panel, in comparison to those found in the COMBO-17 catalog, plotted as a function of the COMBO-17 redshift. In comparison to COMBO-17, even using the same redshifts, the MUSYC data and/or data analysis make galaxies appear brighter and redder, and so more massive.

implies that, at least for $z_{\text{phot}} \lesssim 1$, our results are not seriously affected by our lower photometric redshift accuracy ($\sigma_z \approx 0.03$ for MUSYC, versus 0.02 for COMBO-17, for $R < 24$ and $z_{\text{spec}} < 1$).

To the left of the main panel in Figure B1, we show the difference in (*from top to bottom*) the photometric redshifts, absolute B, and V magnitudes, restframe $(B - V)$ colors, and stellar masses used to produce the solid histograms, and those from the COMBO-17 catalog. In all cases, the ‘ δ ’ is in the sense of ‘MUSYC re-analysis’ minus ‘COMBO-17 catalog’, and is plotted as a function of the COMBO-17 catalog redshift. Within each panel, we also give the biweight mean offset for each quantity, evaluated for sources with $R < 23$ (to reduce random scatter due to photometric uncertainties) and $0.2 < z_{\text{phot}} < 0.5$ (where the COMBO-17 photometry still samples restframe V) in the COMBO-17 catalog.

Looking now briefly at these panels, we see that for $z_{\text{phot}} \gtrsim 0.5$, where the COMBO-17 value for the restframe V magnitude comes from an extrapolation of the best-fit template spectrum, there is a progressive offset between the restframe V luminosities inferred by the MUSYC and COMBO-17 data and analyses—even while using the same redshifts. Even for $z_{\text{phot}} < 0.5$, however, we see a systematic offset of 0.05 mag in $(B - V)$ color. Finally, we note that the greater number of $0.6 < z_{\text{phot}} < 0.8$ galaxies in comparison to $0.2 < z_{\text{phot}} < 0.6$ that we see in the MUSYC data is also present in the COMBO-17 photometric redshift distribution; the difference is that these galaxies do not have $M_* > 10^{11} M_\odot$ in the COMBO-17 catalog.

We therefore conclude that the difference between the COMBO-17 and MUSYC results is not a product of the two surveys’ different photometric redshift accuracies: the use of COMBO-17 rather than MUSYC redshifts affects our results only by a few percent. This leaves the possibilities that the difference between the two results is due to the different methods used to infer galaxies’ restframe properties, or to differences in the data themselves.

B.2. Derivation of Restframe Properties: MUSYC analysis of the COMBO-17 photometry

Are the discrepancies between the COMBO-17 and MUSYC results due to different systematic effects inherent in our different methods for deriving restframe photometry and stellar masses? In order to address this concern, we have reanalyzed the COMBO-17 data using the procedures described in the main text. For this test, in order to isolate the effect of the different analytical methods, we also adopt the COMBO-17 redshift determinations; the difference between this test and the previous one is thus the use of the COMBO-17, rather than the MUSYC, photometry.

The results of this re-analysis are shown as the solid histograms in Figure B2; all other symbols and their meanings are as in Figure B1. The results of the MUSYC re-analysis of the COMBO-17 data agree very well with the COMBO-17 analysis proper: the solid black histogram lies very near the dotted black histogram. Quantitatively, the MUSYC analysis of the COMBO-17 data leads to a red fraction which is 33 % higher than for COMBO-17’s own analysis; the total number density of $M_* > 10^{11} M_\odot$ galaxies agree to better than 1 %.

Comparing the MUSYC- and COMBO-17-derived restframe properties — again, based on the same photometry and redshifts — we do see systematic differences. We make three specific observations: 1. there appear to be discrete redshift regimes where the MUSYC- and COMBO-17-derived restframe fluxes compare differently; 2. for $0.2 \lesssim z_{\text{phot}} \lesssim 0.35$, we see a ‘bimodal’ offset in the MUSYC- and COMBO-17-derived $(B - V)$ colors, corresponding to red and blue galaxies; 3. the MUSYC-derived restframe fluxes appear to be systematically brighter than those derived by COMBO-17, even

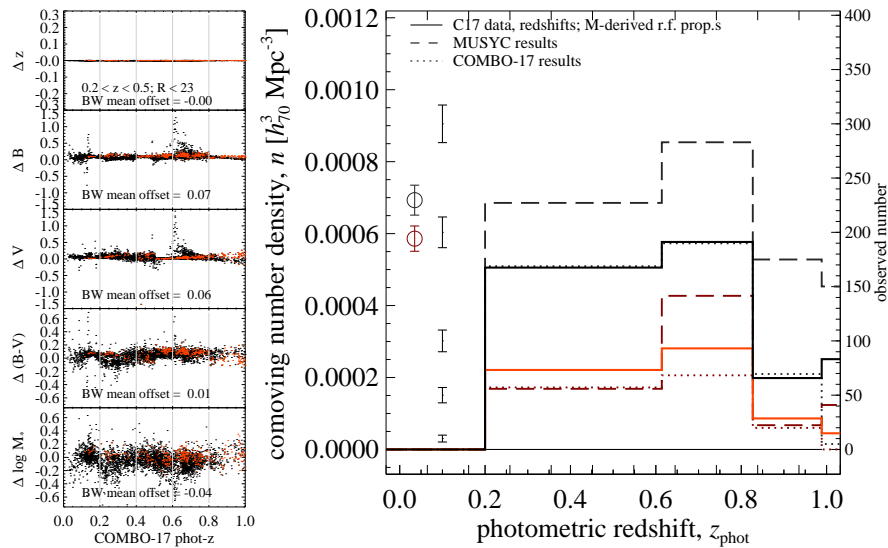


FIG. B2.— MUSYC analysis of the COMBO-17 photometry—The solid histograms in the main panel show the measured number density of $M_* > 10^{11}$ galaxies, applying the MUSYC analysis to the COMBO-17 photometry. In order to isolate the effect on our measurements due to the different methods for deriving restframe properties, we continue to adopt the COMBO-17 redshifts for this test. All other symbols and their meanings are as in Figure B1. Applying the MUSYC analysis to the COMBO-17 photometry, we reproduce the COMBO-17 result to better than 1 %; the difference between the COMBO-17 and MUSYC results cannot be explained solely by our different analytical methods.

for the same photometry. Remarkably, even despite these differences, our stellar mass estimates agree to within 0.04 dex, with a scatter of just 0.11 dex. Finally, we note that the progressive offset in extrapolated V luminosities for $z_{\text{phot}} \gtrsim 0.5$ seen in the previous test is not seen here; that is, applied to the same data, the two techniques for extrapolating restframe photometry yield similar results.

We therefore conclude that the difference between the COMBO-17 and MUSYC results in the ECDFS cannot be explained by differences in the analytical methods employed by each team: the MUSYC reanalysis of the COMBO-17 data agrees with the COMBO-17 fiducial results. Instead, it seems that the different results are really in the data themselves.

B.3. Photometric Calibration: MUSYC analysis of the recalibrated COMBO-17 photometry

A direct, object-by-object comparison of COMBO-17 and MUSYC photometry reveals significant differences in the photometric calibration of the two surveys (Paper I). Specifically, we see differences of 0.00, 0.06, 0.08, 0.08, and 0.14 mag between the MUSYC and COMBO-17 $UBVRI$ -band photometry for galaxies, such that the MUSYC photometry is systematically brighter and redder. This has subsequently been confirmed to be due to an error in the photometric calibration of the COMBO-17 data (Wolf et al. 2008). Can this difference in photometric calibration explain the different results found by COMBO-17 and MUSYC?

To address this issue, we have simply scaled the COMBO-17 photometry to match the MUSYC photometry, and repeated our analysis. The COMBO-17 team has calibrated each of the medium bands relative to the nearest broad band; accordingly we have scaled each of the medium bands by the MUSYC-minus-COMBO-17 offset for the nearest broad band. The results of this test are shown in Figure B3. The MUSYC re-analysis of the recalibrated COMBO-17 photometry agrees extremely well with the fiducial MUSYC results: the measured number density of $M_* > 10^{11} M_\odot$ galaxies at $0.2 < z_{\text{phot}} < 0.8$ agree to better than 1 %.

There are two separate aspects to this re-calibration: galaxies are both brighter and redder in the MUSYC catalog than in COMBO-17. Since COMBO-17 measures total fluxes from their R band image, the 0.08 mag offset between the COMBO-17 and MUSYC zeropoints makes galaxies appear 7.6 % brighter (and thus more massive) in the MUSYC catalog; this effect is responsible for approximately 70 % of the change in the measured number density. At the same time, the reddening of the SED shape implies a higher mass-to-light ratio after recalibration; this effect is responsible for the other 30 % of the change in the measurements.

We therefore conclude that the primary cause for the disagreement between the results of the MUSYC and COMBO-17 surveys in the ECDFS is the different photometric calibrations of the two surveys: reanalyzing the COMBO-17 data set, recalibrated to match the MUSYC photometry, the results agree with the MUSYC fiducial analysis.

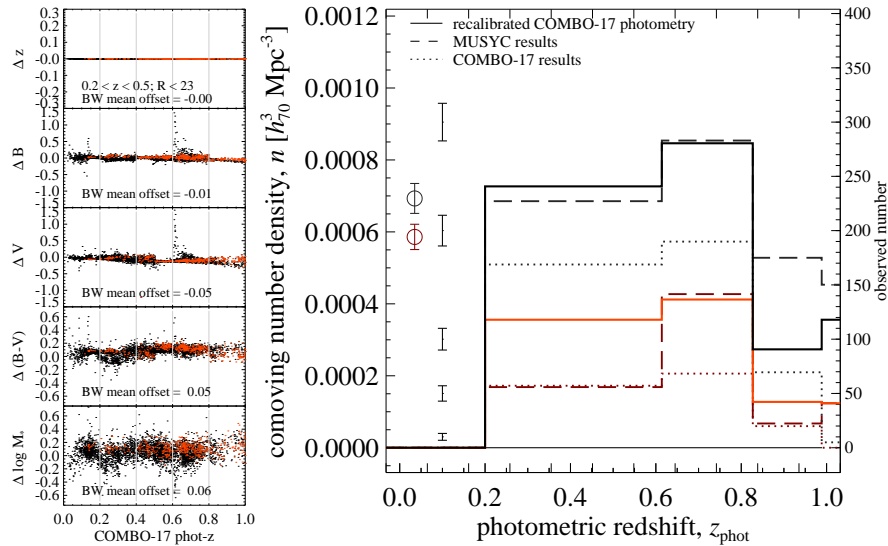


FIG. B3.— Recalibration of the COMBO-17 photometry—the solid histograms in the main panel show the measured number density of $M_* > 10^{11}$ galaxies, applying the MUSYC analysis to the COMBO-17 photometry, recalibrated to match the MUSYC photometry. Specifically, the $UBVRI$ bands have been scaled up by 0.00, 0.06, 0.08, 0.08, and 0.14 mag; each of the medium bands has been scaled to match the nearest broad band. We continue to adopt the COMBO-17 redshifts for this test. All other symbols and their meanings are as in Figure B1. The effect of this rescaling is to increase the measured values by a further 30 %, in comparison to the previous test. Together, the combined effect of this recalibration is nearly 50 %, almost completely explaining the difference between the COMBO-17 and MUSYC results.